The 2dF–SDSS LRG and QSO survey: the QSO luminosity function at 0.4 <z <2.6

Journal Item

Monthly Notices
of the
ROYAL ASTRONOMICAL SOCIETY

Mon. Not. R. Astron. Soc. **399,** 1755–1772 (2009) doi:10.1111/j.1365-2966.2009.15398.x

The 2dF–SDSS LRG and QSO survey: the QSO luminosity function at $0.4 < z < 2.6$

Scott M. Croom,[1⋆] Gordon T. Richards,[2] Tom Shanks,[3] Brian J. Boyle,[4] Michael A. Strauss,[5] Adam D. Myers,[6] Robert C. Nichol,[7] Kevin A. Pimbblet,[8] Nicholas P. Ross,[3,9] Donald P. Schneider,[9] Robert G. Sharp[10] and David A. Wake[3]

[1]*Sydney Institute for Astronomy, School of Physics, University of Sydney, NSW 2006, Australia*
[2]*Department of Physics, Drexel University, Philadelphia, PA 19104, USA*
[3]*Department of Physics, University of Durham, South Road, Durham DH1 3LE*
[4]*Australia Telescope National Facility, PO Box 76, Epping, NSW 1710, Australia*
[5]*Princeton University Observatory, Peyton Hall, Princeton, NJ 08544, USA*
[6]*Department of Astronomy, University of Illinois at Urbana-Champaign, Urbana, IL 61801, USA*
[7]*Institute of Cosmology and Gravitation, Mercantile House, Hampshire Terrace, University of Portsmouth, Portsmouth PO1 2EG*
[8]*Department of Physics, University of Queensland, Brisbane, QLD 4072, Australia*
[9]*Department of Astronomy and Astrophysics, 525 Davey Laboratory, Pennsylvania State University, University Park, PA 16802, USA*
[10]*Anglo-Australian Observatory, PO Box 296, Epping, NSW 1710, Australia*

Accepted 2009 July 15. Received 2009 July 13; in original form 2009 June 12

ABSTRACT

We present the quasi-stellar object (QSO) luminosity function (LF) of the completed 2dF–SDSS LRG and QSO (2SLAQ) survey, based on QSOs photometrically selected from Sloan Digital Sky Survey (SDSS) imaging data and then observed spectroscopically using the 2dF instrument on the Anglo-Australian Telescope. We analyse 10 637 QSOs in the redshift range $0.4 < z < 2.6$ to a g-band flux limit of 21.85 (extinction-corrected) and an absolute continuum magnitude of $M_g(z = 2) < -21.5$. This sample covers an area of 191.9 deg^2.

The binned QSO LF agrees with that of the brighter SDSS main QSO sample, but extends $\sim$2.5 mag fainter, clearly showing the flattening of the LF towards faint absolute magnitudes. 2SLAQ finds an excess of QSOs compared to the 2dF QSO Redshift Survey at $g > 20.0$, as found previously by Richards et al. The LF is consistent with other previous, much smaller, samples produced to the depth of 2SLAQ.

By combining the 2SLAQ and SDSS QSO samples, we produce a QSO LF with an unprecedented combination of precision and dynamic range. With this we are able to accurately constrain both the bright and faint ends of the QSO LF. While the overall trends seen in the evolution of the QSO LF appear similar to pure luminosity evolution, the data show very significant departures from such a model. Most notably we see clear evidence that the number density of faint QSOs peaks at lower redshift than bright QSOs: QSOs with $M_g > -23$ have space densities which peak at $z < 1$, while QSOs at $M_g < -26$ peak at $z > 2$. By fitting simple LF models in narrow M_g intervals, we find that this *downsizing* is significant at the 99.98 per cent level.

We show that LF models which follow the pure luminosity evolution form [i.e. $M^*_g \equiv M^*_g(z)$], but with a redshift-dependent bright-end slope and an additional density evolution term, $\Phi^* \equiv \Phi^*(z)$, provide a much improved fit to the data. The bright-end slope, α, steepens from $\alpha \simeq -3.0$ at $z \simeq 0.5$ to $\alpha = -3.5$ at $z \simeq 2.5$. This steepening is significant at the 99.9 per cent level. We find a decline in Φ^* from $z \simeq 0.5$ to 2.5 which is significant at the 94 per cent level.

⋆E-mail: scroom@physics.usyd.edu.au

Key words: galaxies: active – quasars: general – galaxies: Seyfert.

1 INTRODUCTION

Accurate measurement of the luminosity function (LF) is of prime importance in the study of active galactic nuclei (AGN). One of the key goals of studying AGN is to characterize and understand their strong evolution (e.g. Schmidt 1972; Braccesi et al. 1980; Schmidt & Green 1983; Boyle, Shanks & Peterson 1988, hereafter BSP88; Hewett, Foltz & Chaffee 1993; Boyle et al. 2000; Croom et al. 2004, hereafter C04; Richards et al. 2006, hereafter R06). Early measurements of the quasi-stellar object (QSO) LF demonstrated strong evolution in the population, with luminous QSOs being much more common at high redshift ($z \sim 2$). However, because the shape (at bright magnitudes) is a featureless power law, the type of evolution could not be quantified, i.e. there was no observable difference between density evolution (a change in the number of objects) and luminosity evolution (a change in the luminosities of objects). Surveys which probed fainter than the observed break in the LF (e.g. Boyle et al. 1990, hereafter BFSP90) started to allow some understanding of the physical process behind QSO evolution. These studies showed that QSO evolution approximately followed pure luminosity evolution (PLE), with the same characteristic LF shape evolving to higher luminosities at higher redshift. A naive interpretation of such evolution would imply that QSOs are cosmologically long-lived and fade from $z \sim 2$ to 0. Given their low space density relative to normal galaxies, this also implies that QSOs are intrinsically rare. However, more accurate measurements of the bright end of the QSO LF showed an evolving slope (Hewett et al. 1993; Goldschmidt & Miller 1998; R06), suggesting that QSO evolution did not perfectly follow the PLE model. At redshifts $\gtrsim$2.5, there is an observed decline in the space density of bright QSOs (Osmer 1982; Warren, Hewett & Osmer 1994; Schmidt, Schneider & Gunn 1995; Fan et al. 2001). Thus, $z \simeq 2$–3 is often known as the *quasar epoch*, where QSOs (or quasars) were most active.

The realization that most massive galaxies contain supermassive black holes (SMBHs) (e.g. Kormendy & Richstone 1995) meant that QSOs were likely to be intrinsically common. This result is much more suggestive of a model where QSOs are a short-lived process that occurs in most massive galaxies. The observed evolution is then due to global effects such as a decline in the triggering rate or fuelling of AGN, which modulates the distribution of many successive generations.

Early measurements of the X-ray AGN LF (e.g. Boyle et al. 1993) showed evolution which also approximately followed PLE. However, the most recent X-ray surveys, in particular using *Chandra* (e.g. Giacconi et al. 2002; Alexander et al. 2003) and *XMM–Newton* (e.g. Hasinger et al. 2001; Worsley et al. 2004), reach to much fainter flux levels. These surveys have demonstrated that PLE fails to match the redshift-dependent evolution of the AGN LF at $L < L^*$ (where L^* is the characteristic luminosity at which the QSO LF flattens). They show that the activity in faint AGN peaks at a lower redshift than that of more luminous AGN (e.g. Ueda et al. 2003; Hasinger, Miyaji & Schmidt 2005); this process has been described as AGN downsizing (e.g. Barger et al. 2005). The galaxy population is also seen to undergo a similar downsizing (Cowie et al. 1996), where the most massive galaxies formed the bulk of their stars earlier than lower mass galaxies (e.g. Juneau et al. 2005; Noeske et al. 2007; Zheng et al. 2007).

Given that all massive galaxies contain an SMBH, and that there are tight correlations between black hole mass and host properties (e.g. Tremaine et al. 2002), the growth of black holes and galaxies must be intimately connected. In particular, it has been proposed that galaxy mergers trigger major episodes of star formation (e.g. in ultraluminous infrared galaxies) and lead to QSO activity (Sanders et al. 1988). Such a mechanism can plausibly form spheroidal galaxies and QSOs, and this idea has been further developed by recent numerical simulations (e.g. Hopkins et al. 2005a). In such a picture, accretion on to an SMBH is triggered (at least for moderate- to high-luminosity AGN) by the merger of gas-rich galaxies. While the time-scale for the merger may be $\sim$1 Gyr, for the majority of this time the accretion is obscured from view by dust. Only when the AGN finally expels the surrounding gas and dust does it shine as an optical QSO for a brief period ($\sim$100 Myr), before exhausting its fuel supply (e.g. Di Matteo, Springel & Hernquist 2005). This feedback of energy from the AGN into the host also heats and expels the gas in the galaxy, which suppresses star formation leading to 'red and dead' ellipticals or bulges. One of the key predictions of the Hopkins et al. model is that the faint end of the QSO LF should largely comprise high-mass SMBHs at low accretion rates (i.e. well below their peak luminosity) rather than lower mass SMBHs accreting near the Eddington rate (Hopkins et al. 2005b). Thus, while the bright end of the QSO LF tells us about the intrinsic properties of the QSO population during the time when black holes where increasing in mass most rapidly (e.g. triggering rate, active black hole mass function, etc.), the faint end of the LF tells us about the length of time QSOs spend at relatively low accretion rates.

The 2dF QSO Redshift Survey (2QZ; Croom et al. 2001, 2004) covered an area of 720 deg^2, and reached $\sim$1 mag fainter than the break in the QSO LF at $z < 2$. However, as the observed break in the LF is a relatively gradual flattening towards faint magnitudes, the constraints from the 2QZ on the actual slope of the faint end are uncertain, as demonstrated by the difference between the results from the first release (Boyle et al. 2000) and the final release (C04) of the 2QZ. Samples that reach substantially deeper are required to properly constrain the shape of the faint QSO LF. Such deeper spectroscopic surveys have only covered small areas to date. Wolf et al. (2003) used the medium-band photometric data from the COMBO-17 survey to construct a QSO LF to $R < 24$ that contains $\sim$200 QSOs over an area of 1 deg^2. They provided a measurement of the QSO LF over the redshift range $1.2 < z < 4.8$, but were unable to differentiate between density and luminosity evolution. Jiang et al. (2006) used the deep Sloan Digital Sky Survey (SDSS; York et al. 2000) data from the Fall Equatorial Stripe ('Stripe 82') to construct a sample of 400 QSOs over 4 deg^2 to $g < 22.5$. They found good agreement with the early 2dF–SDSS LRG And QSO (2SLAQ) survey results of Richards et al. (2005, hereafter R05), but were not able to see any clear evidence of downsizing in the AGN population. Using data from the Very Large Telescope (VLT) VIsible MultiObject Spectrograph (VIMOS) Deep Survey (VVDS), Bongiorno et al. (2007) constructed a QSO LF to a limit of $I_{AB} <$ 24 with 130 QSOs in an area of 1.7 deg^2. When combined with the SDSS data from R06, these authors found that their data are better fit by a luminosity-dependent density evolution (LDDE) model, which also matches X-ray samples, suggestive of downsizing.

The 2SLAQ survey (Croom et al. 2009, hereafter C09) was specifically designed to probe the faint end of the QSO LF, reaching approximately 1 mag deeper than the 2QZ. A key requirement of the 2SLAQ survey was that it should cover sufficient area to allow accurate measurement of QSO clustering, as well as to reduce the random errors in the measurement of the LF, spectral properties, etc. Richards et al. (2005) presented the QSO LF from an early 2SLAQ data set using ≃5600 QSOs; this result shows an excess over the 2QZ survey at $g \simeq 21$, but still clearly demonstrates a break in the LF. In this paper, we present the QSO LF for the final 2SLAQ sample. In addition to containing approximately twice as many QSOs, this analysis also makes use of the improved completeness estimates presented by C09, which includes the impact of QSO host galaxies. In Section 2, we briefly describe the 2SLAQ survey. In Section 3, we discuss in detail the issue of *K*-corrections, followed by a calculation of QSO number counts in Section 4. Binned estimates of the QSO LF are presented in Section 5, including a combined 2SLAQ+SDSS LF, and we describe model fits to the data in Section 6. Section 7 discusses our results in the context of recent models for galaxy and QSO evolution. We summarize our conclusions in Section 8. Throughout this paper we assume a cosmological model with $H_0 = 70\,\mathrm{km\,s^{-1}\,Mpc^{-1}}$, $\Omega_\mathrm{m} = 0.3$ and $\Omega_\Lambda = 0.7$. All photometric measurements quoted in this paper have been corrected for Galactic extinction using the maps of Schlegel, Finkbeiner & Davis (1998).

2 THE 2SLAQ SURVEY

The 2SLAQ survey combines *ugriz* (Fukugita et al. 1996) photometry from the SDSS Data Release 1 (Gunn et al. 1998, 2006; Stoughton et al. 2002; Abazajian et al. 2003) and deep spectroscopy using the 2dF spectrograph on the Anglo-Australian Telescope (Lewis et al. 2002). The survey is described in detail by C09. In this section, we summarize the key properties of the sample. QSO candidates are selected with $18.0 < g < 21.85$ [SDSS point spread function (PSF) photometry, extinction-corrected], using a multicolour method which primarily selects ultraviolet (UV)-excess objects. This limits the redshift range to $z \lesssim 3$, with the completeness falling below 50 per cent at $z > 2.6$. QSO candidates fainter than $g = 20.5$ had higher priority when configuring a field for observation with 2dF, as the main focus of the survey was on the faint end of the QSO LF. The 2SLAQ survey covers an area of 191.9 deg^2 in two regions along the celestial equator (declination $= -1\overset{\circ}{.}259$ to $+0\overset{\circ}{.}840$) in the north and south galactic caps (henceforth named the NGP and SGP regions). This area corresponds to a cosmological volume of 4.0 Gpc^3 over the redshift range $0.4 < z < 2.6$ (in our assumed cosmology).

The observations contain new spectra of 16 326 objects, of which 8764 are QSOs. A total of 7623 of these are newly discovered, with the remainder previously identified by the 2QZ (C04) and SDSS (Schneider et al. 2007) surveys. The full QSO sample contains 12 702 QSOs and is presented in C09.

C09 discuss the completeness of the 2SLAQ QSO sample in detail. In particular, because the survey is somewhat fainter than previous large QSO surveys, it is important to take into account the effect of the host galaxy on completeness. C09 showed that QSOs at $z < 1$ near the faint limit of the survey are significantly redder because of the contribution of the host galaxy component, and that this reduces the completeness of the colour selection. This has also been demonstrated in the small but complete sample of QSOs from the VVDS (Gavignaud et al. 2006).

3 THE *K*-CORRECTION

An accurate *K*-correction is required to properly account for the redshifting of the observed passbands when calculating absolute magnitudes or fluxes. In QSO spectra, broad emission lines can also contribute a significant fraction of the flux (typically 0.2–0.5 mag) in a photometric band. As faint targets in the 2SLAQ sample can be affected by their host galaxy, we also need to subtract the host flux to obtain the nuclear component. This is in contrast to most previous samples (e.g. 2QZ, SDSS), where an absolute magnitude limit was applied to the sample, and objects brighter than that limit were assumed not to be significantly affected by flux from their hosts.

3.1 Correcting for host galaxy flux

The detailed completeness simulations described by C09 enable correction of the 2SLAQ QSO magnitudes for their mean host galaxy contributions. The photometric data used to select QSOs are the SDSS PSF magnitudes, so this will already limit the host galaxy flux to some extent (e.g. Schneider et al. 2003). However, C09 demonstrated that at low luminosity the host galaxies of the 2SLAQ sample can still significantly alter their observed colours. We use the modelled host properties presented by C09 to correct the 2SLAQ QSOs for the contribution of their host galaxies. For each simulated source, C09 calculate the total, nuclear- and host-only magnitudes. We can then derive the mean correction from total to nuclear magnitude in *g* and *z* intervals (note that here, and throughout this paper, *z* denotes redshift and not a magnitude in the SDSS *z* band). This is shown in fig. 16a and table 12 of C09. In the *g* band, in which the 2SLAQ sample was selected, the host contribution is less than 20 per cent at $z > 0.4$, even for the faintest sources. Thus, corrections for the host galaxy have only a limited effect on the measured QSO LF.

3.2 The QSO *K*-correction

Several studies have determined *K*-corrections for QSOs. Typically, to *K*-correct to $z = 0$, a power-law correction of the form $K(z) = -2.5(1 + \alpha_\nu)\log_{10}(1 + z)$ has been used, with $\alpha_\nu \simeq -0.5$. While QSOs have an underlying power-law continuum, the broad emission lines in their spectra have a significant impact on the total flux in a given band. Cristiani & Vio (1990), in their *K*-correction analysis, include the impact of emission lines using composite QSO spectra. Wisotzki (2000) derived *K*-corrections from the optical/UV spectrophotometry of QSOs made available by Elvis et al. (1994). This study resulted in a *K*-correction that is substantially steeper at low redshift ($z < 0.5$) than other work, flattening to a more typical power law at higher redshift. R06 suggested removing the emission-line contributions to the flux before determining a luminosity. This gives a more direct measurement of the energy output from the central engine, unbiased by the location of the passband with respect to the QSO emission-line spectrum. Following R06, we also correct for the emission-line flux and construct an emission-line *K*-correction, K_em. The emission-line *K*-correction includes a contribution from emission lines to the *g*-band flux at $z = 0$ (predominantly Hβ, Hγ, [O III] and some iron emission) and thus is not zero at $z = 0$. To determine K_em, we take a median of the emission-line *K*-corrections derived from the simulated QSO spectra constructed by C09. In this emission-line *K*-correction, we also include the effect of Lyman α forest absorption.

It is also useful to normalize the K-correction closer to the median redshift of the sample (e.g. Blanton et al. 2003), to minimize the extrapolation required for the bulk of the objects. Although the mean redshift of the 2SLAQ sample is $z \sim 1.4$, we will normalize our K-corrections to $z = 2$ in order to be consistent with R06. This $z = 2$ g-band K-correction acts as a g-band filter with the wavelengths divided by $(1 + z)$. To obtain a total K-correction, we then add a power-law component with $\alpha_\nu = -0.3$. This power-law slope is slightly different from the standard $\alpha_\nu = -0.5$ usually assumed, but was found to give the best match to observed QSO colours in the simulations of C09.

A comparison of different K-correction estimates in the literature is shown in Fig. 1(a). In the cases which do not explicitly include the $z = 0$ emission-line correction we have added this contribution, so that these provide K-corrections to a continuum magnitude at $z = 0$. The QSO K-corrections normalized at $z = 0$ increasingly diverge towards high redshift. In contrast, if we normalize the K-corrections at $z = 2$ (Fig. 1b), the K-corrections are much more consistent over the redshift range we are sampling, $z \simeq 0.4$–2.6. We note that the 2SLAQ K-corrections and those of Wisotzki (2000) match very well, apart from at $z = 0$. However, there is a substantial difference between the emission-line-only components of these K-corrections (Fig. 1c). We attribute this difference to the difficulty of defining the *true* continuum regions of QSO spectra, as opposed to regions which are just free from the major emission lines, but which may still contain significant contributions from iron lines and other weaker emission features.

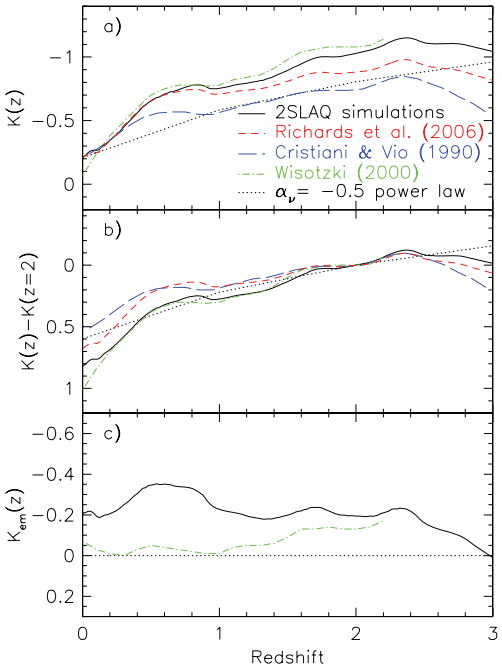

Figure 1. (a) The g-band QSO K-corrections normalized to the continuum at $z = 0$ from the 2SLAQ simulations of C09 (solid black line), R06 (short dashed red line), Cristiani & Vio (1990) (long dashed blue line), Wisotzki (2000) (dot–dashed green line) and a power law with $\alpha_\nu = -0.5$ (dotted black line). The Cristiani & Vio K-correction has been transformed from their B- and V-band measurements to the g band. The 2SLAQ K-correction comprises an emission-line component and a power law with $\alpha_\nu = -0.3$. The R06, Cristiani & Vio and power-law K-corrections have been shifted by -0.209 to correct for the $z = 0$ emission-line contribution. This has not been done to the Wisotski K-correction which already includes an emission-line term. The emission-line contribution causes these K-corrections not to pass through zero at $z = 0$, even though they are normalized at $z = 0$. (b) The same K-corrections, but normalized at $z = 2$. (c) The emission-line K-corrections from our work (black solid line) and Wisotzki (2000) (green dot–dashed line).

In our analysis below we will use our K-corrections (black line in Fig. 1), and correct to the continuum flux in the g band at $z = 2$. The emission-line contribution at this redshift is 0.194 mag, such that $M_{g,\mathrm{cont}}(z = 2) = M_{g,\mathrm{total}}(z = 2) + 0.194$. R05 used a more traditional K-correction, zero-pointed at $z = 0$, assuming a power law with $\alpha_\nu = -0.5$ and no emission-line correction. Averaged over the sample at $z = 0.3$–2.2, we find that we need to subtract 0.41 from the R05 absolute magnitudes to match our new K-corrections (with a maximum variation with redshift of ± 0.1 mag). We find that an identical correction of -0.41 is needed to transform the Cristiani & Vio (1990) K-corrections on to our new K-corrections. In some cases below, we will be required to use the different K-corrections discussed above to compare our results to those of previous authors.

4 QSO NUMBER COUNTS

We first calculate the number counts of QSOs as a function of g magnitude. The raw QSO counts from the 2SLAQ sample are shown in Fig. 2 (open squares). The filled squares show the number counts corrected for coverage completeness only, i.e. fraction of targets in our survey region which were actually observed. The coverage completeness is known exactly, while other completeness corrections (e.g. photometric selection, spectroscopic completeness; see C09 for details) have some uncertainties. The fully corrected counts (in the redshift range $0.4 < z < 2.1$) are shown by the open and filled circles (for the NGP and SGP regions, respectively). We see no significant difference between the NGP and SGP regions. Fig. 3 compares the number counts from the preliminary 2SLAQ sample (R05) to our current determination. In order to directly compare the two, we use the same K-correction and M_g limit as R05, namely, a power-law K-correction, normalized at $z = 0$ with $\alpha_\nu = -0.5$ and a limit of $M_g < -22.5$. We also do not make any correction for the host galaxy contribution to the total flux, as this was not done by

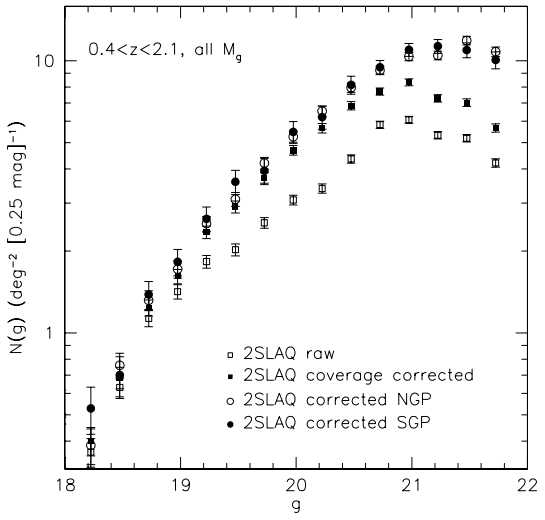

Figure 2. The g-band QSO number counts from the 2SLAQ survey at $0.4 < z < 2.1$ (with no absolute magnitude limits). In this plot, we compare the raw counts (open squares) and counts corrected for coverage completeness only (filled squares) to the counts after applying all corrections (coverage, photometric, spectroscopic, etc.; see C09) in the NGP and SGP regions separately (open and filled circles).

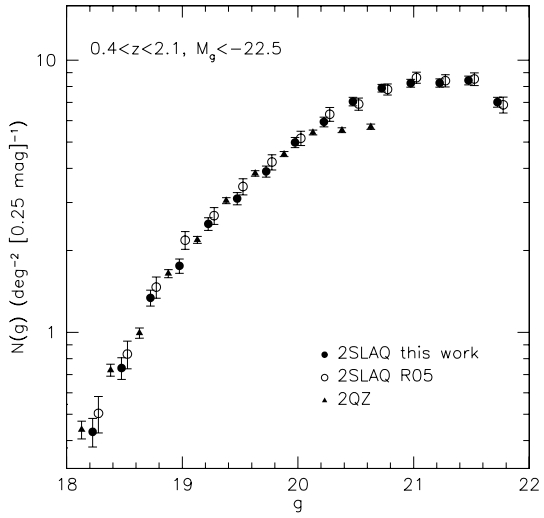

Figure 3. The g-band QSO number counts from the final 2SLAQ survey at $0.4 < z < 2.1$ (filled circles) compared to the previous estimate from R05 (open circles) and the 2QZ sample (C04; filled triangles; assuming $g = b_J - 0.045$). All samples are limited to $M_g < -22.5$ (or $M_{b_J} < -22.5$). The final 2SLAQ points (filled circles) have been calculated using a $z = 0$ power-law K-correction with $\alpha_\nu = -0.5$ to match R05. The 2QZ points use the Cristiani & Vio (1990) K-correction which is very close to the $\alpha_\nu = -0.5$ version. The new and old estimates from 2SLAQ agree well. They also agree with 2QZ at $g < 20$, but fainter than this 2QZ has significantly lower counts. The drop in the faintest magnitude bin for 2SLAQ is largely due to the $M_g < -22.5$ limit which preferentially removes the faintest sources.

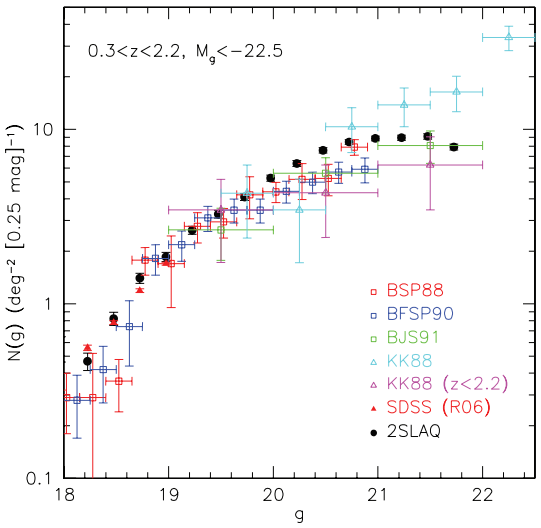

Figure 4. The g-band QSO number counts from the final 2SLAQ survey (filled circles) at $0.3 < z < 2.2$ ($M_g < -22.5$; $\alpha_\nu = -0.5$ K-correction) compared to other samples. We show number counts from R06 (SDSS DR3) in the g band (filled red triangles); BSP88 (open red squares); BFSP90 (open blue squares); Boyle et al. (1991, hereafter BJS91; open green squares); KK88 (open cyan triangles); KK88 $z < 2.2$, taken from the table of BJS91 (open magenta triangles).

R05. Despite the different photometric completeness estimates used in our work and R05, there is excellent agreement between the two estimates of the 2SLAQ $n(g)$ distribution. In particular, the decline at the faintest magnitudes is present in both analyses. This drop is mostly due to the absolute magnitude cut which preferentially removes objects at the faintest magnitudes.

In Fig. 3, we also compare the 2SLAQ $n(g)$ to that derived from the 2QZ sample (C04). As noted by R05, the 2SLAQ counts are an excellent match to 2QZ at $g < 20$, but at fainter magnitudes 2SLAQ contains an increasingly higher density of QSOs than does 2QZ, with this excess reaching ∼25 per cent at the faintest bin of the 2QZ. We discuss this discrepancy between 2SLAQ and 2QZ number counts in further detail in Section 7.1. In Fig. 4, we compare the 2SLAQ number counts (again using the $z = 0, \alpha_\nu = -0.5$ power-law K-correction and $M_g < -22.5$) to a wide range of previously published number counts. This includes the main SDSS sample (R06; filled red triangles), which is only plotted at $g < 19$, after which incompleteness strongly affects the g-band number counts (as the sample is selected in the i band). We also show the older number counts of BSP88 and BFSP90. These have a similar depth to 2QZ and are also consistently below 2SLAQ at $g > 20$. The deeper sample of Boyle, Jones & Shanks (1991) is in agreement with 2SLAQ (albeit with large errors), while the full Koo & Kron (1988, hereafter KK88) sample, not limited to $z < 2.2$, lies above 2SLAQ. As pointed out by R05, the number count for the subsample of KK88 QSOs limited to $z < 2.2$ is significantly lower, and is below or consistent with 2SLAQ (although the KK88 sample is also restricted to $z > 0.9$). Overall there is good agreement between these various analyses; however, the redshift ranges and limits of these different samples do not always match exactly. Detailed comparison to more recent estimates of the QSO LF will be presented below.

5 THE LUMINOSITY FUNCTION

In Fig. 5, we show the distribution of 2SLAQ sources in the z–M_g plane, applying the $z = 2$ g-band continuum K-correction described in Section 3.2. When we use M_g hereafter we will be using this as shorthand for continuum $M_g(z = 2)$. Using this sample, we first calculate the binned LF using the model-weighted estimator suggested by Miyaji, Hasinger & Schmidt (2001). This improves on the $1/V$ estimator devised by Page & Carrera (2000), which partially

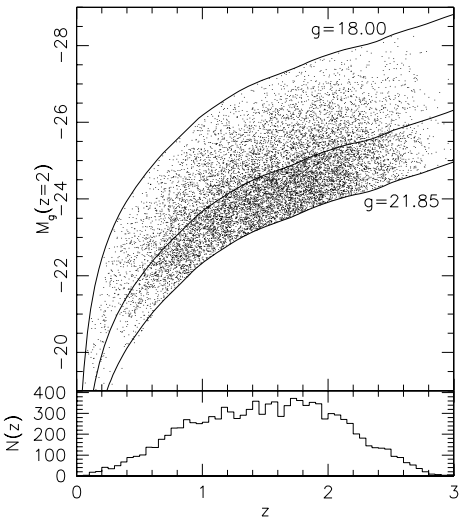

Figure 5. The $M_g(z = 2)$ versus z distribution for the 2SLAQ sample, applying the K-correction described in Section 3.2 (g-band continuum, normalized at $z = 2$). Each object is corrected for a statistical contribution from its host galaxy. The top and bottom solid lines denote the 2SLAQ apparent magnitude limits at $g = 18.0$ and 21.85 (not corrected for the host contribution). The middle solid line indicates $g = 20.5$ boundary between our bright and faint samples. The objects fainter than the flux limit at low redshifts are due to the host galaxy correction.

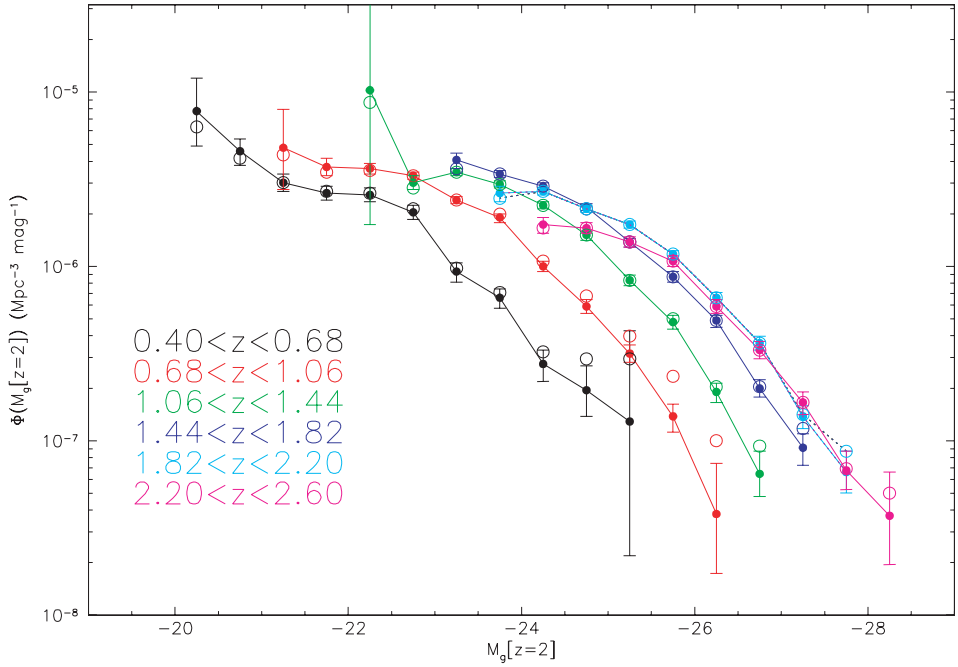

Figure 6. The binned 2SLAQ LF for six redshift intervals from $z = 0.4$ to 2.6. The filled points are those derived using the model-weighted estimator described in the text. The open points are derived using the Page & Carrera (2000) estimator which accounts for the flux limits crossing the bins, but does not account for the change in source density within a bin.

corrects for binning effects, but assumes a uniform distribution across each bin. The model-weighted estimator uses the best model fit to the *unbinned* LF data (described in Section 6) to correct for the variation of the LF within a bin, which is particularly critical at the steep bright end of the QSO LF. This estimator gives the binned LF as

$$\Phi(M_{g,i}, z_i) = \Phi(M_{g,i}, z_i)^{\rm model} \frac{N_i^{\rm obs}}{N_i^{\rm model}}, \quad (1)$$

where $M_{g,i}$ and z_i are the absolute magnitude and redshift at the centre of the ith bin. $\Phi(M_{g,i}, z_i)^{\rm model}$ is the best-fitting model evaluated at $M_{g,i}$ and z_i. $N_i^{\rm obs}$ is the number of observed QSOs in the bin and $N_i^{\rm model}$ is the number estimated from the model (accounting for completeness corrections). In the LFs presented here, we use the luminosity evolution + density evolution (LEDE) model fits described in Section 6.4, although assuming a PLE model fit does not produce a significant difference to the estimate of the binned LF.

Fig. 6 shows the binned 2SLAQ LF for six different redshift intervals from $z = 0.4$ to 2.6. This binning matches the redshift intervals from the SDSS Data Release 3 (DR3) LF of R06, except that we have increased the lowest redshift limit from 0.3 to 0.4, which is the lowest redshift at which we trust our completeness corrections. The 2SLAQ LF shows the approximate characteristics of PLE, i.e. a fixed LF shape with an evolving L^*. However, there is also evidence for deviations from a PLE model, including variation in slope and normalization which we will investigate below. The open points in Fig. 6 show the binned LF using the $1/V$ Page & Carrera (2000) estimator. This demonstrates that at the steep bright end of the QSO LF, the $1/V$ estimator can cause significant bias.

5.1 Comparison to the SDSS LF and a combined 2SLAQ–SDSS LF

In Fig. 7, we compare the 2SLAQ LF to that derived for the brighter SDSS DR3 sample by R06. As both analyses K-correct to a continuum-only magnitude, we can convert from the $M_i(z = 2)$ magnitudes of R06 with

$$M_g(z = 2) = M_i(z = 2) + 2.5\alpha_\nu \log\left(\frac{4670\ \text{Å}}{7471\ \text{Å}}\right). \quad (2)$$

In Fig. 7, we assume $\alpha_\nu = -0.5$. We plot the LF in six different panels, and the dotted lines show the $1.82 < z < 2.20$ LF as a comparison. The SDSS DR3 LF (open circles) is a smooth continuation of the 2SLAQ LF towards higher luminosities. This figure clearly shows the QSO LF break. This break is a gradual flattening of the QSO LF, which starts at approximately the faint limit of the main SDSS QSO sample.

We next combine the 2SLAQ and SDSS data sets to produce a single, binned, g-band LF with unprecedented precision and dynamic range. This is done by taking the QSO sample presented by R06, including the completeness estimates. The R06 LF is presented in the i band, as this is the band which provides the flux limit for the SDSS QSO sample. To combine this data with the 2SLAQ sample, we need to convert the selection function (table 1 of R06) from the i band to the g band, and specify an appropriate range in g-band flux over which to calculate the LF. To convert the selection function to the g band, we calculate the median $g - i$ colours of SDSS QSOs as a function of redshift, z. This is then used to map the completeness in each (i band, z) interval to the corresponding (g band, z) interval. The (g band, z) completeness is then resampled on to a uniform grid. To obtain suitable flux limits for the SDSS sample in the g band, we examine the $g - i$ colours of SDSS QSOs as a function of g (for all redshifts; Fig. 8). The i-band flux limits imposed on the SDSS QSO sample (solid diagonal lines in Fig. 8) mean that at faint g-band magnitudes the bluest QSOs will be missed. We apply a faint limit of $g = 18.7$, which does not cause any QSOs to be rejected on the basis of their $g - i$ colour, as there are virtually no QSOs bluer than $g - i = -0.4$ in the SDSS sample. At the bright end, there are no bright $z > 0.3$ QSOs ($g \lesssim 17$) which are redder than $g - i = 0.5$.

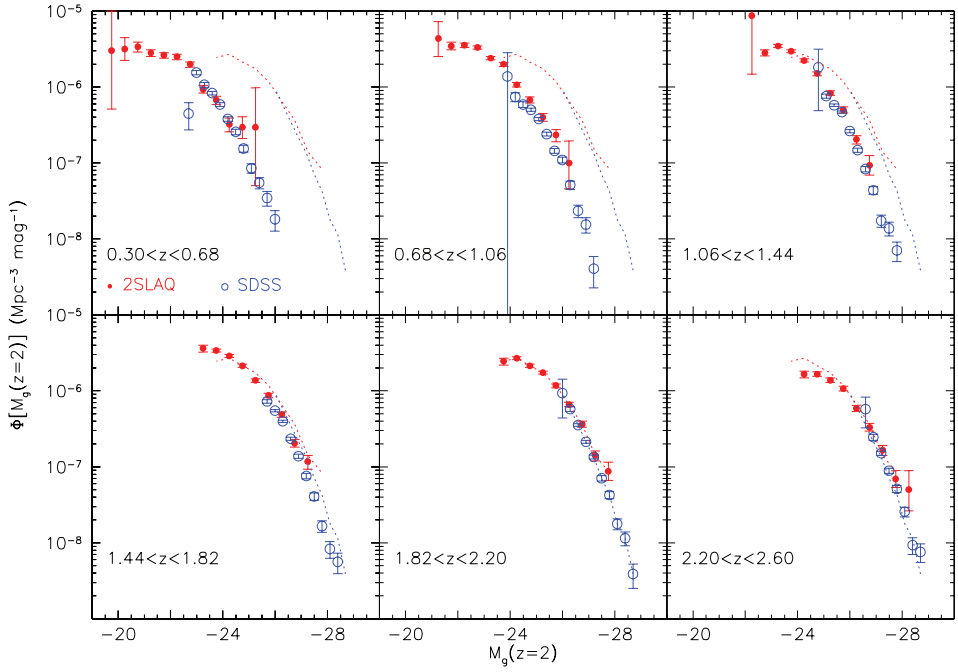

Figure 7. The binned 2SLAQ LF (filled red points) for six redshift intervals from $z = 0.3$ to 2.6, compared to the SDSS LF (R06; blue open points). The dotted lines show the LFs at $1.82 < z < 2.20$ as a reference.

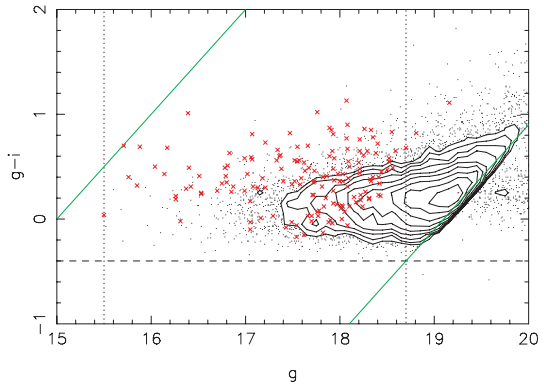

Figure 8. The $g - i$ colours versus g of SDSS QSOs from the DR3 LF sample of R06. The black points and contours are SDSS QSOs at $z > 0.3$, while the red crosses are at $z < 0.3$. The contours are logarithmically spaced, based on the density of points per 0.1 by 0.1 mag bin, starting at log(density) = 1.0, with steps of 0.17. The diagonal solid (green) lines mark the SDSS flux limits at $i = 15.0$ and 19.1. The horizontal dashed line marks the limit of $g - i = -0.4$, below which there are virtually no QSOs. The vertical dotted lines indicate our chosen g-band limits of $g = 15.5$ and 18.7.

Those at $z < 0.3$ are systematically redder (red crosses in Fig. 8), due to the contribution of their host galaxy. However, we are not considering the QSO LF below $z = 0.3$, therefore we can safely ignore this population. We therefore set the bright limit at $g = 15.5$ (cf. the SDSS i-band bright limit of $i = 15.0$).

Applying the appropriate flux limits and completeness corrections, we then combine the SDSS and 2SLAQ samples to produce the binned LF in Fig. 9 (using the model-weighted estimator). This LF covers a much greater dynamic range that either the SDSS or 2SLAQ samples do on their own. One point to note is that the binning has a non-trivial effect on the LF of the combined data set, near the overlap of the two samples. The model-weighted LF estimator accurately corrects for these binning biases, and it is this estimator that is shown in Fig. 9. The LF values and associated errors are listed in Table 1.

In Fig. 10, we plot the space density of QSOs from the combined 2SLAQ+SDSS sample as a function of redshift in narrow M_g slices. At bright absolute magnitudes ($M_g \lesssim -27$), the space density of QSOs is monotonically increasing up to $z \simeq 2.5$. However, the space density of fainter QSOs peaks at lower redshift, e.g. $z \simeq 1.6$ for $M_g = -23.5$. This is in disagreement with PLE, in which the space density of QSOs peaks at the same redshift at every luminosity. This is the same trend that has been seen in previous X-ray-selected samples of AGN and has been called 'AGN downsizing' (e.g. Barger et al. 2005; Hasinger et al. 2005). This downsizing was first seen in X-ray samples because they were the first to have the dynamic range and object numbers to allow it to be measured.

5.2 Comparison to other observed LFs

Fig. 11 presents a comparison of our combined 2SLAQ and SDSS LF to that measured from the 2QZ survey by C04. To convert from b_J- to g-band magnitude, we use $g - b_J = -0.045$ as found by R05. We then take into account the difference between our current K-correction and that used by C04, giving $M_g(z = 2) = M_{b_J} - 0.455$ (averaged over redshift). In general, there is excellent agreement between the LFs measured from the two samples. In the lowest redshift interval ($0.4 < z < 0.68$), the 2QZ LF appears slightly higher than the 2SLAQ data at $M_g \simeq -24$, which we attribute to the fact that the K-correction used by C04 (derived from the work of Cristiani & Vio 1990) is flatter at low redshift than our assumed K-correction (see Fig. 1). A shift of only ∼0.1 mag is sufficient to bring the 2QZ and 2SLAQ data into excellent agreement here. In all other redshift intervals, the agreement between 2QZ and 2SLAQ is very good, with the exception of the faintest ∼1 mag of the 2QZ LF, which is significantly lower than the 2SLAQ LF at all redshifts. This is consistent with the difference seen in the number counts presented in Section 4. In Fig. 11, we also plot the preliminary 2SLAQ LF

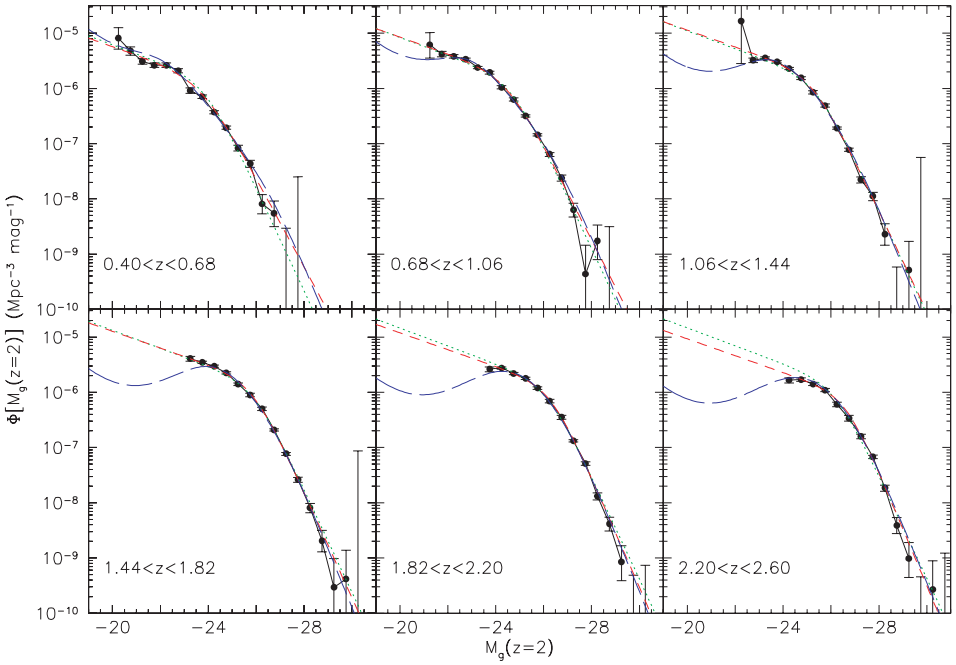

Figure 9. The combined 2SLAQ and SDSS g-band LF for six redshift intervals from $z = 0.4$ to 2.6, estimated using the model-weighted method. The error bars without visible points are upper limits, i.e. no QSOs were found, although the accessible volume was non-zero. We compare the measured LF to the best PLE model (green dotted lines), smooth LDDE model (blue long dashed lines) and LEDE model (red short dashed lines).

calculated by R05 (green triangles). We offset this LF by −0.41 mag to account for the difference between our K-correction and the $z = 0$, $\alpha_\nu = -0.5$ power-law K-correction used by R05. The R05 2SLAQ LF and our current work are in excellent agreement, even though the completeness estimates have been significantly revised, and different K-corrections are assumed. This gives us confidence that any remaining uncertainties in our photometric completeness or effects due to the K-correction are unlikely to significantly bias our LF estimates.

In Figs 12 and 13, we compare the 2SLAQ+SDSS result to other LF measurements at faint fluxes. While these reach fainter fluxes than 2SLAQ, they are constructed from smaller samples and so have much larger uncertainties. The COMBO-17 LF (Wolf et al. 2003) is shown in Fig. 12, with the 2SLAQ+SDSS LF rebinned to the same redshift intervals. The COMBO-17 LF is defined in the M_{1450} passband using Vega magnitudes, which is close to the g band at $z = 2$. The equivalent of equation (2) then gives $M_g(z = 2) = M_{1450} + 1.216$ for $\alpha_\nu = -0.5$, after correcting from Vega to AB (Oke & Gunn 1983) magnitudes. Applying this correction gives the COMBO-17 LF plotted in Fig. 12. We see good agreement between 2SLAQ and COMBO-17 where they overlap. The COMBO-17 LF is slightly lower than the 2SLAQ LF in the $1.20 < z < 1.80$ interval. However, given the size of the error bars and possible remaining uncertainty in the flux transformation, we do not consider this significant.

Jiang et al. (2006) determine the QSO LF using a sample of 414 QSOs covering an area of 3.9 deg^2 limited to $g < 22.5$. This sample was selected from co-adds of the multi-epoch Stripe 82 SDSS data. Jiang et al. clearly demonstrate the flattening of the QSO LF towards faint magnitudes, but do not have sufficient precision to measure any downsizing effect. Jiang et al. use a K-correction which is derived separately for each object, but that is zero-pointed to $z = 0$. To correct the Jiang et al. magnitudes, we assume that they are well approximated by a simple $\alpha_\nu = -0.5$ power-law K-correction and apply an offset of −0.41 to move them to our $M_g(z = 2)$ system. The comparison of our 2SLAQ+SDSS LF with the result of Jiang et al. is shown in Fig. 13. There is good agreement between the two data sets, although at $0.5 < z < 1.0$ the Jiang et al. LF is somewhat lower than the 2SLAQ+SDSS LF.

Another recent determination of the faint end of the QSO LF is from the VVDS (Bongiorno et al. 2007). A comparison between 2SLAQ and VVDS is shown in Fig. 13. The VVDS LF is determined in the B band. To convert to our $M_g(z = 2)$ band, we use

$$M_g(z = 2) = M_B(z = 0) - 2.5(1 + \alpha_\nu)\log(3) - 0.14 + 0.209, \quad (3)$$

where −0.14 arises from the mean difference between the B and g bands for QSOs (R06) and the +0.209 comes from the emission-line contribution. This results in a correction of $M_g(z = 2) = M_B(z = 0) - 0.527$ for $\alpha_\nu = -0.5$. The 2SLAQ and VVDS LFs are again in good general agreement, except for the faintest two 2SLAQ bins in the $1.0 < z < 1.5$ redshift interval, where the VVDS point is significantly higher than 2SLAQ. The 2SLAQ points in this region are marginally lower than those at brighter luminosities, possibly suggesting some unaccounted-for incompleteness. However, these 2SLAQ points are in good agreement with the result of Jiang et al. (2006). Given the uncertainties due to small numbers in the VVDS sample and issues such as cosmic variance, it is not clear that there is a true disagreement. Future comparison with the final VVDS sample, covering a larger area, should aid in the resolution of this issue.

We next compare to the X-ray LF of Hasinger et al. (2005), which is a soft X-ray LF of type 1 AGN from a combined sample of ∼1000 objects in the 0.5–2.0 keV band. We convert from our $M_g(z = 2)$ band to the 0.5–2.0 keV band, largely following R05. The g-band luminosity is given by

$$\log[L_g(z = 0)] = -0.4M_g(z = 2) + 20.638, \quad (4)$$

Table 1. Binned LF for the combined 2SLAQ and SDSS sample using the model-weighted estimator, as plotted in Fig. 9. We give the value of log Φ in six redshift intervals, and in $\Delta M_g = 0.5$ mag bins. We also list the mean redshift ($\bar{z}$) in each bin, the number of QSOs contributing to the LF (N_Q) and the lower and upper errors (Δ log Φ). At the bright end of the LF, some bins contain no QSOs, even though the accessible volume is non-zero. In this case, the values in the log Φ column are 1σ Poisson upper limits on the LF in this bin.

	$0.40 < z < 0.68$					$0.68 < z < 1.06$					$1.06 < z < 1.44$				
M_g	$\bar{z}$	N_Q	log Φ	Δ log Φ		$\bar{z}$	N_Q	log Φ	Δ log Φ		$\bar{z}$	N_Q	log Φ	Δ log Φ	
−29.75	–	0	–	–	–	–	0	–	–	–	–	0	−7.25	–	–
−29.25	–	0	–	–	–	–	0	–	–	–	1.31	1	−9.31	−0.77	+0.52
−28.75	–	0	–	–	–	–	0	−8.50	–	–	–	0	−9.23	–	–
−28.25	–	0	–	–	–	1.02	3	−8.85	−0.34	+0.29	1.25	7	−8.65	−0.20	+0.19
−27.75	–	0	−7.60	–	–	0.77	1	−9.42	−0.77	+0.52	1.30	34	−7.96	−0.08	+0.07
−27.25	–	0	−8.53	–	–	0.97	15	−8.25	−0.13	+0.12	1.29	69	−7.65	−0.06	+0.05
−26.75	0.56	5	−8.28	−0.24	+0.22	0.94	57	−7.67	−0.06	+0.05	1.30	254	−7.11	−0.03	+0.03
−26.25	0.60	8	−8.10	−0.18	+0.17	0.92	158	−7.24	−0.04	+0.03	1.24	431	−6.73	−0.02	+0.02
−25.75	0.58	43	−7.37	−0.07	+0.06	0.92	354	−6.88	−0.02	+0.02	1.20	260	−6.32	−0.03	+0.03
−25.25	0.57	81	−7.09	−0.05	+0.05	0.85	369	−6.52	−0.02	+0.02	1.27	194	−6.08	−0.03	+0.03
−24.75	0.58	200	−6.71	−0.03	+0.03	0.83	262	−6.22	−0.03	+0.03	1.28	300	−5.82	−0.03	+0.02
−24.25	0.54	250	−6.44	−0.03	+0.03	0.90	173	−6.00	−0.03	+0.03	1.27	448	−5.65	−0.02	+0.02
−23.75	0.50	185	−6.16	−0.03	+0.03	0.90	287	−5.72	−0.03	+0.02	1.26	555	−5.53	−0.02	+0.02
−23.25	0.54	77	−6.04	−0.05	+0.05	0.90	342	−5.62	−0.02	+0.02	1.24	484	−5.46	−0.02	+0.02
−22.75	0.56	121	−5.69	−0.04	+0.04	0.87	421	−5.48	−0.02	+0.02	1.14	118	−5.52	−0.04	+0.04
−22.25	0.58	141	−5.59	−0.04	+0.04	0.83	274	−5.44	−0.03	+0.03	1.07	1	−4.99	−0.77	+0.52
−21.75	0.55	119	−5.58	−0.04	+0.04	0.75	81	−5.43	−0.05	+0.05	–	0	–	–	–
−21.25	0.52	81	−5.52	−0.05	+0.05	0.70	5	−5.32	−0.24	+0.22	–	0	–	–	–
−20.75	0.49	33	−5.34	−0.08	+0.07	–	0	–	–	–	–	0	–	–	–
−20.25	0.45	7	−5.11	−0.20	+0.19	–	0	–	–	–	–	0	–	–	–

	$1.44 < z < 0.82$					$1.82 < z < 2.20$					$2.20 < z < 2.60$				
M_g	$\bar{z}$	N_Q	log Φ	Δ log Φ		$\bar{z}$	N_Q	log Φ	Δ log Φ		$\bar{z}$	N_Q	log Φ	Δ log Φ	
−30.25	–	0	–	–	–	–	0	–	–	–	–	0	−9.81	–	–
−30.25	–	0	−7.06	–	–	–	0	−9.13	–	–	2.21	1	−9.58	−0.77	+0.52
−29.75	1.76	1	−9.40	−0.77	+0.52	–	0	−9.31	–	–	–	0	−9.34	–	–
−29.25	1.48	1	−9.54	−0.77	+0.52	2.03	3	−9.08	−0.34	+0.29	2.51	3	−9.02	−0.34	+0.29
−28.75	1.67	7	−8.69	−0.20	+0.19	2.03	15	−8.38	−0.13	+0.12	2.45	12	−8.42	−0.15	+0.14
−28.25	1.65	28	−8.09	−0.09	+0.08	2.01	47	−7.89	−0.07	+0.06	2.38	61	−7.74	−0.06	+0.05
−27.75	1.66	90	−7.58	−0.05	+0.04	2.02	193	−7.30	−0.03	+0.03	2.37	212	−7.17	−0.03	+0.03
−27.25	1.66	285	−7.11	−0.03	+0.02	1.99	387	−6.88	−0.02	+0.02	2.33	108	−6.81	−0.04	+0.04
−26.75	1.61	541	−6.68	−0.02	+0.02	1.99	150	−6.47	−0.04	+0.03	2.38	73	−6.48	−0.05	+0.05
−26.25	1.61	195	−6.32	−0.03	+0.03	2.00	185	−6.18	−0.03	+0.03	2.36	119	−6.23	−0.04	+0.04
−25.75	1.65	226	−6.06	−0.03	+0.03	2.01	285	−5.93	−0.03	+0.02	2.39	201	−5.97	−0.03	+0.03
−25.25	1.64	313	−5.86	−0.03	+0.02	2.01	432	−5.76	−0.02	+0.02	2.37	277	−5.86	−0.03	+0.03
−24.75	1.65	510	−5.66	−0.02	+0.02	2.00	538	−5.67	−0.02	+0.02	2.38	265	−5.78	−0.03	+0.03
−24.25	1.63	635	−5.54	−0.02	+0.02	1.99	557	−5.57	−0.02	+0.02	2.31	103	−5.76	−0.05	+0.04
−23.75	1.63	528	−5.47	−0.02	+0.02	1.91	101	−5.58	−0.05	+0.04	–	0	–	–	–
−23.25	1.52	98	−5.39	−0.05	+0.04	–	0	–	–	–	–	0	–	–	–

assuming $\alpha_\nu = -0.3$. We then convert to rest-frame luminosity at 2500 Å via

$$\log(L_{2500}) = \log[L_g(z=0)] - 0.3 \log\left[\frac{4670}{2500}\right] \quad (5)$$

and convert to monochromatic luminosity at 2 keV using

$$\log(L_{2\,\mathrm{keV}}) = \log(L_{2500}) + \alpha_{\mathrm{ox}} \log\left(\frac{\nu_{2\,\mathrm{keV}}}{\nu_{2500}}\right). \quad (6)$$

The α_{ox} parameter is the slope between 2500 Å and 2 keV. Various measurements show that this is dependent on luminosity; we use the bisector method result of Steffen et al. (2006), which gives

$$\alpha_{\mathrm{ox}} = -0.107 \log(L_{2500}) + 1.740. \quad (7)$$

Finally, we integrate over the 0.5–2.0 keV band assuming a photon index of $\Gamma = 2.0$. This produces a final conversion of

$$\log(L_{0.5-2\,\mathrm{keV}}) = 36.972 - 0.288 M_g. \quad (8)$$

In Fig. 14, we plot the comparison between the X-ray LF of Hasinger et al. (2005) and our combined 2SLAQ+SDSS LF. These LFs overlap in the redshift intervals $0.4 < z < 0.8$ and $0.8 < z < 1.6$. Overall, there is impressive agreement between the optical and X-ray LFs. This agreement is best close to the break in the LF, with the X-ray LF lying slightly above the optical LF at both fainter and brighter magnitudes. The bright-end slope of the X-ray LF is somewhat flatter than the optical LF. We test how the luminosity dependence of α_{ox} impacts this by taking a generalized form of equation (8): $\log(L_{0.5-2keV}) = A - B M_g$. We fit for A and B by finding the values which bring the X-ray and optical LFs into the closest agreement. We find $B = 0.362 \pm 0.023$, which infers a significantly weaker luminosity dependence for α_{ox} than is found by Steffen et al. (2006).

6 MODEL FITS

As described above, the binned LF can be a biased estimator whenever the LF changes significantly over the size of the bin (e.g. at

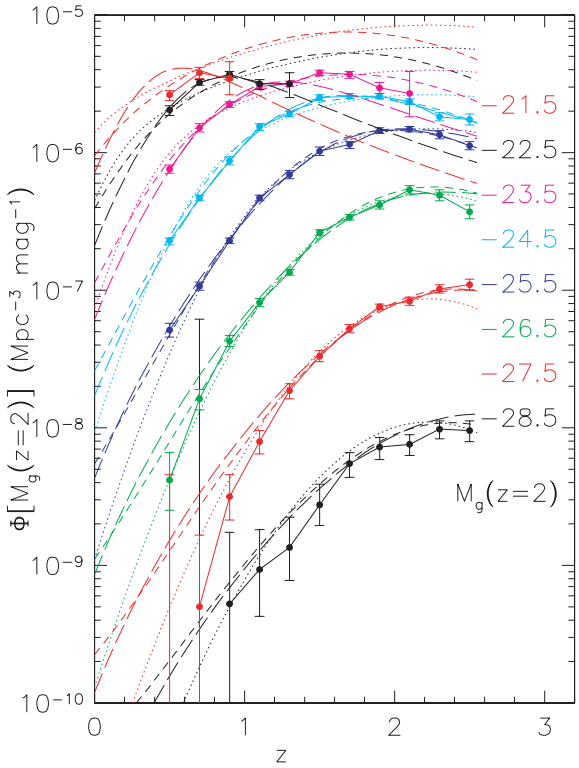

Figure 10. The combined 2SLAQ and SDSS LF (using the model-weighted method) plotted as a function of redshift for different M_g intervals. The brightest intervals are at the bottom of the plot and the faintest at the top. Each M_g interval is connected by a solid line apart from points which are upper limits (e.g. $M_g = -27.5$, $z = 0.5$). To aid the clarity of this plot, the small number of noisy points at $M_g = -29.5$ and -30.5 have been omitted. We compare the measured LF to the best-fitting PLE model (dotted lines), smooth LDDE model (long dashed lines) and LEDE model (short dashed lines).

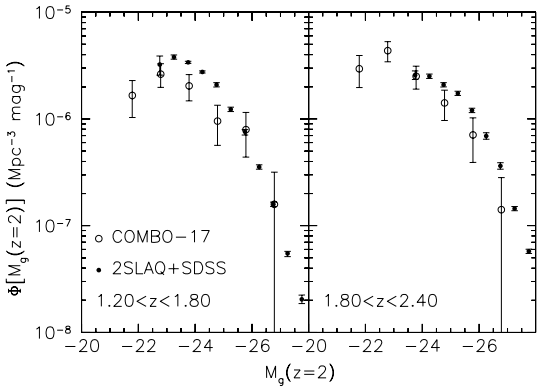

Figure 12. The binned 2SLAQ+SDSS LF (filled circles) compared to Wolf et al. (2003) (COMBO-17; open circles).

the steep bright end of the LF). Therefore, a parametric QSO LF is also usually derived by performing a maximum likelihood (ML) fit to the unbinned data using the method first proposed by Marshall et al. (1983). The key issue in such fitting is to choose a functional form which is representative of the data. Optical QSO LFs have previously been well fit by PLE models, and so we will start by considering this parametrization. Then we will investigate other forms such as LDDE.

The ML approach has one disadvantage: the normalization of the LF, $\Phi^* \equiv \Phi(M_g^*)$, cannot be determined directly from the fitting. We therefore estimate this after the fitting process by integrating over the best-fitting model, such that

$$\Phi^* = \frac{N_{\rm Q}}{\int_{M_{\rm min}}^{M_{\rm max}} \int_{z_{\rm min}}^{z_{\rm max}} \frac{\Phi(M,z)}{\Phi^*} A(M) \frac{{\rm d}V}{{\rm d}z} {\rm d}M {\rm d}z}, \quad (9)$$

where $N_{\rm Q}$ is the total number of QSOs, $A(M)$ is the effective area of the survey (which is a function of magnitude if combining different samples; i.e. 2SLAQ and SDSS), ${\rm d}V/{\rm d}z$ is the cosmological

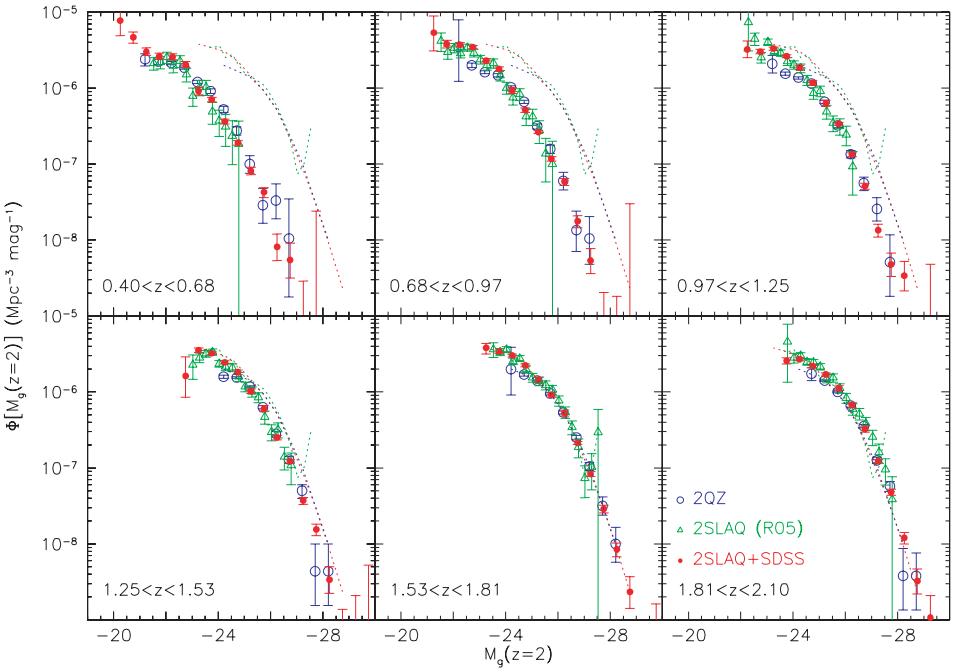

Figure 11. The binned 2SLAQ+SDSS LF for six redshift intervals from $z = 0.4$ to 2.1 (filled red points), compared to the 2QZ LF of C04 (open blue circles) and the preliminary 2SLAQ LF of R05 (open green triangles). The dotted lines show the LFs at $1.53 < z < 1.81$ as a reference.

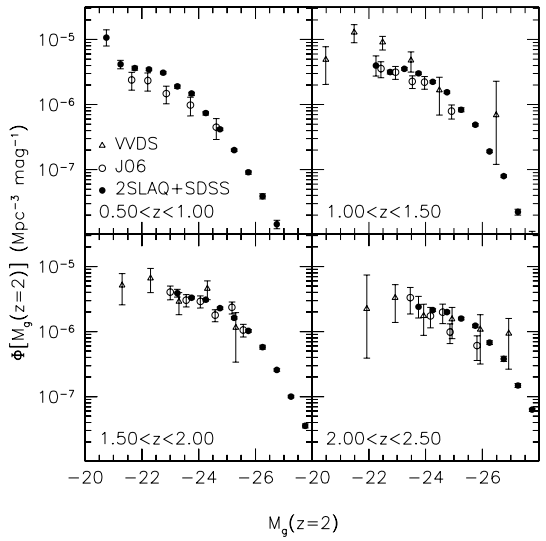

Figure 13. The binned 2SLAQ+SDSS LF (filled circles) compared to the LFs of Jiang et al. (2006) (open circles) and Bongiorno et al. 2007 (VVDS, open triangles). Note that the VVDS LF is not plotted for $0.5 < z < 1.0$, as Bongiorno et al. did not calculate it in this redshift interval.

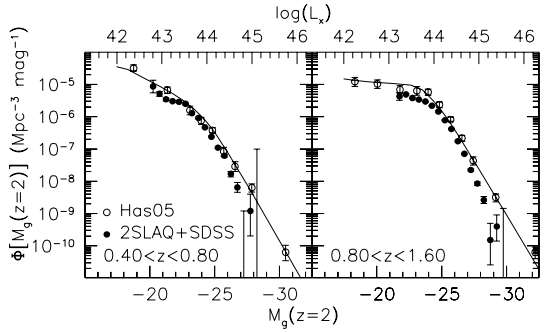

Figure 14. The binned 2SLAQ LF (filled points) compared to the X-ray LF of Hasinger et al. (2005; open points). The 2SLAQ LF has been recalculated in the redshift ranges presented by Hasinger et al. The solid line denotes the LDDE model fit made by Hasinger et al. to their data.

volume element and $\Phi(M, z)/\Phi^*$ is the result of the ML fitting process. The uncertainties in Φ^* arise from the Poisson error in N_Q and the uncertainties in the fitted model parameters; the latter is the dominant term in our case. The Φ^* error is given by the maximum range of the Φ^* values from model parameter sets that are within the 1σ N-dimensional confidence contours of the ML fit (e.g. for five parameters, within a region where $\Delta\chi^2 < 5.89$).

A significant issue in the ML process is deciding on the range of redshift and absolute magnitude over which to perform the fitting. The depth of the 2SLAQ data, combined with the detailed completeness estimates at faint magnitudes, allows us to fit to fainter limits than those used by C04 and R05 for the 2QZ and preliminary 2SLAQ analyses, respectively. Therefore, we fit all the QSOs with $M_g(z = 2) < -21.5$. We will also test the impact of applying a limit of $M_g(z = 2) < -23.0$, which is approximately equivalent to the C04 and R05 limit. In redshift, we constrain our fitted range to be $z > 0.4$, as at lower redshift our photometric selection completeness is less certain (see C09). At the high-redshift end, we fit our data up to $z = 2.6$; above this redshift, the photometric selection completeness drops below 50 per cent. In order to fully constrain both the bright and faint ends of the QSO LF, we fit the models to the combined 2SLAQ+SDSS LF.

In assessing the goodness of fit for each model, we will measure the χ^2 value comparing the number of QSOs in a bin and the number predicted by the best-fitting model (after accounting for incompleteness). As the unbinned maximum likelihood fitting method makes use of a Poisson probability distribution function, the best-fitting model will not necessarily correspond to that with the minimum χ^2 (which assumes a Gaussian probability distribution). The binning used to calculate our χ^2 values can also have an impact on the resulting values. As we tend to smaller bins the estimated numbers will be dominated by shot-noise. With larger bins, containing more QSOs, any systematic error and/or mismatch of the model will increase χ^2. As a result, the calculated χ^2 values should be treated as relative assessments of the goodness of fit, rather than absolute ones. We choose to use absolute magnitude bins with $\Delta M_g = 0.5$ and divide the LF into six uniform redshift intervals over the range fitted. As a second independent statistical test, which does not depend on binning, we also apply a two-dimensional Kolmogorov–Smirnov (KS) test (Peacock 1983). This test compares the model LF to the distribution of QSOs in the M_g–z plane.

6.1 Pure luminosity evolution fits

We assume the standard double power law of the form

$$\Phi(M_g, z) = \frac{\Phi\left(M_g^*\right)}{10^{0.4(\alpha+1)(M_g - M_g^*)} + 10^{0.4(\beta+1)(M_g - M_g^*)}}, \quad (10)$$

where Φ is the comoving space density of QSOs. The redshift dependence is characterized purely by evolution in M_g^*. We follow Boyle et al. (2000) by parametrizing this evolution as a second-order polynomial in redshift such that

$$M_g^*(z) = M_g^*(0) - 2.5\left(k_1 z + k_2 z^2\right). \quad (11)$$

We note that this functional form for $M_g^*(z)$ requires symmetric evolution about the brightest M_g^* value. This is likely to break down at redshifts well above the peak (e.g. R06), but our sample is not able to probe to these redshifts.

The resulting best-fitting parameters for the PLE models (equations 10 and 11) are listed in Table 2. The PLE model is a relatively poor fit to the data at $M_g(z = 2) < -21.5$ and $0.4 < z < 2.6$. A χ^2 comparison of the unbinned ML fit to the binned data (after correcting for incompleteness in the bins) gives $\chi^2/\nu = 256.6/80$. The most significant discrepancies between the data and the model are at the faint end of the LF, particularly at high redshift. This is seen in Fig. 9 where the PLE model (green dotted line) is compared to the binned LF. The qualitative agreement actually appears good for a substantial fraction of the LF, even though the overall agreement is poor due to the small statistical errors on the LF measurements. If we restrict the redshift range being fit, then we obtain a significant improvement, with χ^2/ν of 190.8/81 for $0.4 < z < 2.3$ and 181.4/81 for $0.4 < z < 2.1$. Reducing the magnitude range to $M_g < -23$ makes a further improvement to the fitting, giving $\chi^2/\nu = 152.1/72$. The two-dimensional KS tests show a similar trend, although the KS probabilities of acceptance are on average higher. The full redshift and magnitude range have a KS probability of acceptance of only 2.8e–5, while the most restricted data set has a KS probability of $\simeq$3 per cent, and thus is marginally acceptable (at the $\simeq 2\sigma$ level). One of the reasons for the poor fits is shown in Fig. 10, where we find that the space density of fainter QSOs peaks at lower redshift.

Table 2. The best-fitting PLE models (equations 10 and 11). Listed are the redshift ranges and faint M_g limit of the data fitted, the number of QSOs in the analysis (N_Q) and the best-fitting values of the model parameters. We also give the results of comparing the model to the data via χ^2 and KS tests, including the number of degrees of freedom (ν).

Redshift range	M_g limit	N_Q	α	β	M_g^*	k_1	k_2	$\log(\Phi^*)$ Mpc^{-3} mag^{-1}	χ^2	ν	P_{χ^2}	D_{KS}	P_{KS}
0.4–2.1	−21.5	12 977	-3.29 ± 0.04	-1.37 ± 0.04	-22.09 ± 0.09	1.44 ± 0.03	-0.319 ± 0.011	-5.79 ± 0.07	181.4	81	1.2e–09	0.014	6.2e–2
0.4–2.1	−23.0	11 702	-3.38 ± 0.05	-1.48 ± 0.04	-22.36 ± 0.10	1.39 ± 0.04	-0.300 ± 0.010	-5.90 ± 0.08	152.1	72	1.1e–07	0.017	2.6e–2
0.4–2.3	−21.5	14 146	-3.33 ± 0.04	-1.42 ± 0.03	-22.18 ± 0.08	1.44 ± 0.03	-0.315 ± 0.008	-5.84 ± 0.07	190.8	81	7.5e–11	0.019	1.4e–3
0.4–2.6	−21.5	15 073	-3.33 ± 0.04	-1.41 ± 0.03	-22.17 ± 0.08	1.46 ± 0.02	-0.328 ± 0.007	-5.84 ± 0.07	256.6	80	2.2e–20	0.025	2.8e–5

6.2 Luminosity-dependent density evolution fits

We next investigate whether an LDDE model, as first suggested by Schmidt & Green (1983), provides an improvement in χ^2 compared to PLE. We use the model described by Hasinger et al. (2005) and others, which, when expressed in absolute magnitudes, takes the form

$$\Phi(M_g, z) = \frac{A e_d(M_g, z)}{10^{0.4(\alpha+1)(M_g - M_g^*)} + 10^{0.4(\beta+1)(M_g - M_g^*)}}, \quad (12)$$

where A provides the normalization. In this case, M_g^* does not evolve, and the evolution is given by the term

$$e_d(M_g, z) = \begin{cases} (1+z)^{p_1} & \text{if } z \le z_c, \\ (1+z_c)^{p_1}[(1+z)/(1+z_c)]^{p_2} & \text{if } z > z_c, \end{cases} \quad (13)$$

with

$$z_c(M_g) = \begin{cases} z_{c,0} 10^{-0.4\gamma(M_g - M_{g,c})} & \text{if } M_g \ge M_{g,c}, \\ z_{c,0} & \text{if } M_g < M_{g,c}. \end{cases} \quad (14)$$

This model does not provide an improved fit (over PLE) to our combined 2SLAQ+SDSS data set. Fitting over the range $0.4 < z < 2.6$ and $M_g < -21.5$ gives a $\chi^2/\nu = 256.6/77$ (eight free parameters), compared to $\chi^2/\nu = 256.6/80$ for a PLE model (five free parameters) over the same interval. As suggested by Hasinger et al. (2005), we also add a luminosity-dependent term to the power-law exponents p_1 and p_2 in equation (13) such that

$$p_1(M_g) = p_{1,24} - \epsilon_1(M_g + 24), \quad (15)$$

$$p_2(M_g) = p_{2,24} - \epsilon_2(M_g + 24), \quad (16)$$

where the normalization is at $M_g = -24$. A model fit which includes these extra terms also fails to make a significant improvement on the quality of fit ($\chi^2/\nu = 255.6/75$).

When we compare the above LDDE model to the binned LF, a substantial part of the disagreement appears to arise from the piecewise nature of the functional form, which causes sudden changes in the shape of the model. Therefore, we modify the above LDDE model so that the functions describing the evolution are smoothly varying, rather than the piecewise descriptions given by equations (13) and (14). The functional form we choose is similar in shape to the piecewise model and described by

$$e_d(M_g, z) = \frac{2(1+z_c)^{p_1}}{[(1+z)/(1+z_c)]^{-p_1} + [(1+z)/(1+z_c)]^{-p_2}}, \quad (17)$$

where

$$z_c(M_g) = \frac{z_{c,0}}{1 + 10^{0.4\gamma(M_g - M_{g,c})}}. \quad (18)$$

This form of the LDDE model provides a much improved fit over the piecewise form used by H05 (with the same number of degrees of freedom). We find $\chi^2/\nu = 146.8.3/77$ when fitting to QSOs at $0.4 < z < 2.6$ and $M_g < -21.5$. The KS test suggests that the model and data are in agreement at the $\sim$2 per cent level, although the χ^2-test rejects the model at much higher significance. As above, including further terms to allow p_1 and p_2 to vary with magnitude (equations 15 and 16) does not improve χ^2. The best-fitting smooth LDDE model parameters are listed in Table 3 and the model is plotted in Figs 9 and 10 (long dashed lines). From Fig. 10, we can see that the advantage this model has over PLE is that the space density of fainter sources peaks at lower redshift. In this model, the faint-end slope is not fixed, but varies as a function of both redshift and luminosity. This causes the dip and then upturn seen at $z > 1$ in Fig. 9 beyond the range of the data. Such changes in shape beyond the limits of the data should not be taken seriously and are unlikely to be real.

Table 3. The best-fitting LDDE model for $0.4 < z < 2.6$ and $M_g(z=2) < -21.5$. 15 073 QSOs were used in the fit. We also give the results of comparing the model to the data via χ^2 and KS tests, and include the number of degrees of freedom (ν).

Parameter	Value
α	-3.70 ± 0.06
β	-2.34 ± 0.03
M_g^*	-26.69 ± 0.16
$M_{g,c}$	-23.90 ± 0.14
γ	0.68 ± 0.02
$z_{c,0}$	2.47 ± 0.05
p_1	6.28 ± 0.18
p_2	-2.85 ± 0.21
log (A)	-9.21 ± 0.18
χ^2	146.8
ν	77
P_{χ^2}	2.9e–6
D_{KS}	0.015
P_{KS}	1.7e–2

6.3 Fitting narrow M_g and z intervals

While the LDDE model provides an improved fit over PLE, we now explore different forms of the QSO LF which may provide a better match to our data. We start by using the unbinned ML approach to fit the space density of QSOs as a function of redshift in narrow M_g slices of full width $\Delta M_g = 0.5$. A single power law in luminosity with quadratic density evolution is used,

$$\Phi(M_g, z) = \frac{\Phi^* 10^{[Az(1-0.5z/z_p)]}}{10^{0.4(\alpha+1)M_g}}, \quad (19)$$

where we fit for α, A and z_p. For a single power law, the quadratic evolution in density is equivalent to the quadratic evolution in M_g^* described by equation (11). We have reparametrized this so that one of the parameters (z_p) gives the redshift of the peak of the QSO space density. This allows measurement of the peak redshift, z_p, as a function of M_g which is plotted in Fig 15. This figure quantitatively shows the trend that is apparent in Fig. 10 and demonstrates that we see AGN downsizing at high significance. At the extremes of the M_g distribution, the restricted redshift range of the data (due to the flux limited nature of the sample; see dotted lines in Fig. 15) may be biasing our estimate of the peak redshift, but brighter than $M_g = -24$, where the redshift coverage is uniform, we see a consistent trend of increasing z_p with luminosity. The best-fitting linear relation is $z_p = (-6.94 \pm 0.16) + (-0.352 \pm 0.007)M_g$, so the gradient is non-zero at a highly significant level. A Spearman rank correlation test finds that z_p and M_g are correlated at 99.98 per cent significance. The low-luminosity AGN with $M_g > -23$ peak in space density below $z \simeq 1$ and the peak redshift increases monotonically up to the most luminous sources we sample. At $M_g > -26$, the points are consistently below the best-fitting linear relation. This corresponds to $z \simeq 2.2$, but may be biased by the $z \simeq 2.6$ redshift cut-off in our sample. The reality of such a flattening of the peak redshift could be confirmed by faint QSO samples that probe to higher redshift, such as the AAOmega–UKIDSS[1]–SDSS (AUS) Survey currently underway at the Anglo-Australian Telescope (Croom et al., in preparation). In Fig. 15, we also plot $z_c(M_g)$ from the LDDE model (equation 18). This shows increasing peak redshift for brighter QSOs, although $z_c(M_g)$ is typically between 0.2 and 0.4 lower than the directly measured z_p. This is due to the different functional forms fit in each case (quadratic versus double power law).

[1] UKIRT Infrared Deep Sky Survey.

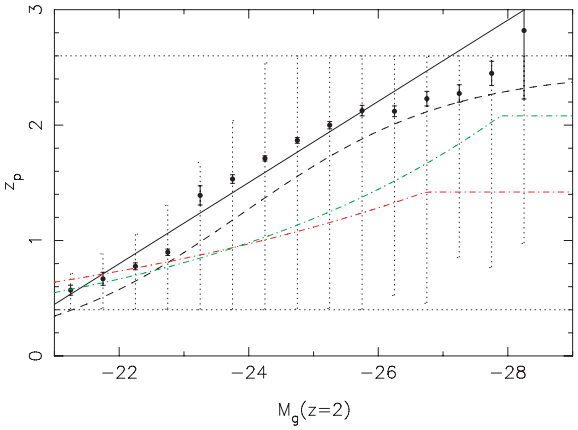

Figure 15. The redshift, z_p, at which the space density of QSOs peaks as a function of M_g. This is determined by fitting equation (19) to our data in narrow slices of full width $\Delta M_g = 0.5$ mag. The horizontal dotted lines indicate the nominal redshift range that was fitted over ($z = 0.4$–2.6), while the vertical dotted lines show the actual redshift range for each M_g bin. The solid line shows the best linear fit and the dashed line is the best-fitting $z_c(M_g)$ using the LDDE model (equation 18). The dot–dashed lines show the evolution of z_c found by Hasinger et al. (2005; red dot–dashed line) and Bongiorno et al. (2007; green dot–dashed line) when fitting a piecewise form of the LDDE model to X-ray and optical data, respectively.

If the completeness of the 2SLAQ sample was overestimated at the faintest magnitudes, this could mimic downsizing. In order to examine this possibility we redetermine the binned LF, but applying a faint flux limit of $g = 21.0$ to our sample. The LF limited at brighter magnitudes is completely consistent with that derived from the full sample. Indeed, the magnitude intervals at $M_g = -24.5$ and -25.5 still show a distinct flattening and turnover (Fig. 10), which is not seen at brighter absolute magnitudes.

We next fit a simple double power law (i.e. equation 10) to the data in narrow redshift intervals, $\Delta z = 0.1$. Over this narrow range, we do not allow for any evolution, and so fit for only three parameters: α, β and M^*. We also derive a fourth parameter, Φ^*, which cannot be fit for using the ML method, but is derived from equation (9). The fitted parameters are shown as a function of redshift in Fig. 16. There is covariance between the fitted parameters for a given redshift slice. However, for a given parameter the measurements between different redshift slices are independent. Fig. 16 shows significant trends with redshift which are inconsistent with PLE. In Fig. 16(a), the bright-end slope, α, shows significant (99.9 per cent from a Spearman rank test) steepening with increased redshift, in agreement with previous results (e.g. Goldschmidt & Miller 1998; C04; R06). Hopkins, Richards & Hernquist (2007) also find a significant change of α at $z \lesssim 2$, which is described by the dotted line in Fig. 16(a). This is inconsistent with our measurement of the evolution of α at the 98 per cent level (via a χ^2-test between the Hopkins et al. model and our data points), although it shows the same general trend. The faint-end slope (β; Fig. 16b) is consistent with no evolution; this is in contrast to the measurement of Hopkins et al. (2007). This difference may be due to our redshift limit of $z > 0.4$, as Hopkins et al. find the steepest values of β below this redshift. Again, a χ^2-test between our data and the Hopkins

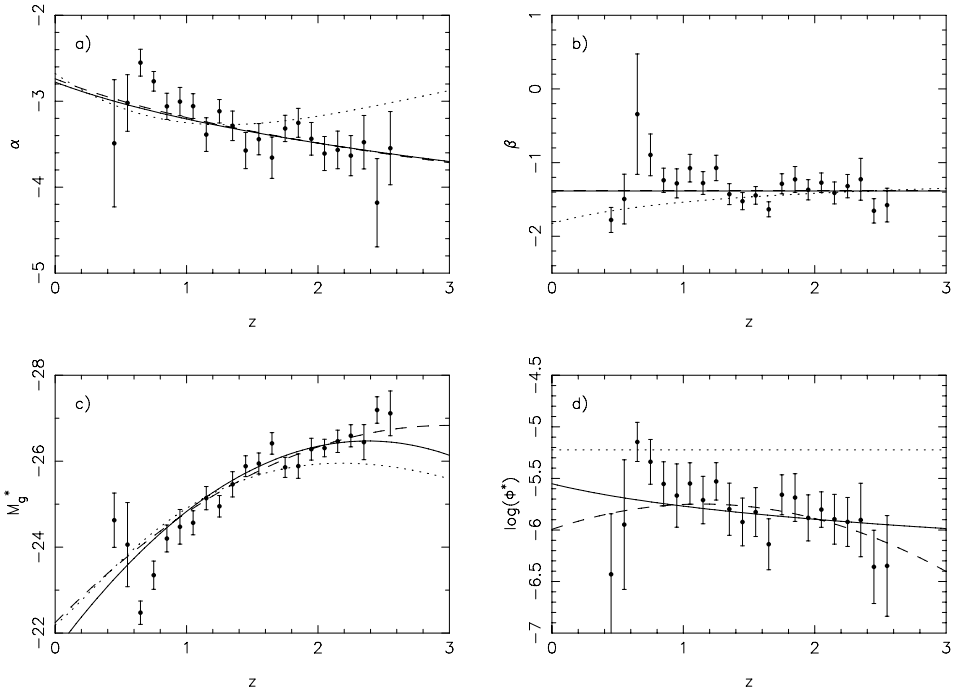

Figure 16. LF parameters for fits of a double power law in narrow redshift slices. (a) The bright-end slope, α, which shows a significant steepening towards high redshift. At redshifts higher than $z \sim 3$, the bright-end slope has been shown by R06 to flatten again. (b) The faint-end slope, β, which shows no significant change as a function of redshift. (c) M_g^*, which shows the well-known strong brightening towards high redshift. (d) The normalization, Φ^*, which shows a systematic reduction towards high redshift. The dotted lines show the best-fitting models derived by Hopkins et al. (2007). The solid and dashed lines show the best fits from our LEDE model, assuming power law and quadratic evolution for Φ^*, respectively.

et al. model is inconsistent at the 98 per cent level. The best-fitting value of M_g^* (Fig. 16c) shows the strong evolution expected in a PLE model, but we also see a systematic decline in Φ^* (Fig. 16d) which is not part of the standard PLE model. The correlation between Φ^* and z is significant at the 94 per cent level from a Spearman rank correlation test. The lowest two redshift bins in Fig. 16 appear to have fitted values which lie off the trend defined by the values at other redshifts; Φ^* is lower, M^* is brighter and α is steeper. If we ignore these two lowest redshift bins then the significance of the correlation between Φ^* and z increases to 99.96 per cent. The above results suggest several modifications to the PLE model which should improve the fit of the model; we investigate this possibility below. The Hopkins et al. model for M_g^* and Φ^* is also plotted (dotted lines) in Figs 16(c) and (d). While the overall trend for M_g^* is the same, the Hopkins et al. model is somewhat flatter. The Hopkins et al. fit for Φ^* is systematically $\simeq$0.4 dex higher than our measurements [after converting from $\mathrm{d}\Phi/\mathrm{d}\log(L)$ to $\mathrm{d}\Phi/\mathrm{d}M$]. A possible cause of this offset is that Hopkins et al. fit their models to a broad range of *binned* data, rather than the unbinned model fits carried out here.

6.4 Modified PLE fits

The first modification we make to the standard PLE model described in Section 6.1 is to allow the bright-end slope, α, to vary with redshift. We follow a parametrization similar to that of Hopkins et al. (2007) and use

$$\alpha(z) = \alpha_{\mathrm{ref}} \left(\frac{1+z}{1+z_{\mathrm{ref}}} \right)^{p_\alpha}, \tag{20}$$

where z_{ref} is fixed at $z_{\mathrm{ref}} = 2$. Hopkins et al. (2007) used a double power law to track the flattening of α at $z > 3$. As our sample does not probe to this redshift, we use a single power-law parametrization.

We account for the evolution in Φ^* seen in Fig. 16(d) using a power-law parametrization such that

$$\Phi^*(z) = \Phi^*_{\mathrm{ref}} \left(\frac{1+z}{1+z_{\mathrm{ref}}} \right)^{p_\Phi}. \tag{21}$$

Again, we take $z_{\mathrm{ref}} = 2$. Fitting this model over the full redshift range ($0.4 < z < 2.6$) and at $M_g < -21.5$ results in a $\chi^2/\nu = 213.3/78$ and $P_{\mathrm{KS}} = 1.9\mathrm{e}{-4}$. This is an improvement over PLE, but not as good as the LDDE model. In Fig. 16, we compare this model fit (solid lines) to the dependencies of α, β, M_g^* and Φ^* with redshift. This model provides a much improved description of the evolving bright-end slope, α, and normalization, Φ^*. In order to further improve the model fit, we try a different parametrization for the evolution in Φ^*. This is a quadratic form, similar to the evolution of M^* in equation (11), such that

$$\log(\Phi^*) = \log\left(\Phi_0^*\right) + [k_{\Phi 1} z (1.0 - 0.5 z / k_{\Phi 2})]. \tag{22}$$

Adding this functional form allows a significant improvement in the fit over the full redshift range, with $\chi^2/\nu = 121.0/77$ and $P_{\mathrm{KS}} = 0.30$. We call this final model luminosity evolution + density evolution (LEDE), and it is plotted in Figs 9 and 10 (short dashed lines). The best-fitting parameters are listed in Table 4. The most notable difference between this model and PLE is the change in amplitude at high redshift and the bright-end slope change. The evolution of Φ^* has the effect of shifting the peak space density of low-luminosity QSOs towards lower redshift, i.e. downsizing (see Fig. 10). The results of the LEDE fit are also shown as the dashed lines in Fig. 16. The evolution in Φ^* is best fit by a quadratic which is convex, i.e. it declines at both low and high redshifts. The power-law and quadratic forms for the evolution in Φ^* are in reasonable agreement over most of the redshift range fitted. However, outside of this range they diverge markedly. This highlights the danger of

Table 4. The best-fitting modified LEDE model (i.e. using equations 20 and 22) for $0.4 < z < 2.6$ and $M_g(z = 2) < -21.5$. 15 073 QSOs were used in the fit. We also give the results of comparing the model to the data via χ^2 and KS tests, and include the number of degrees of freedom (ν).

Parameter	Value
$\alpha_{\rm ref}$	-3.48 ± 0.05
p_α	0.220 ± 0.018
β	-1.38 ± 0.03
M_g^*	-22.24 ± 0.09
k_1	1.23 ± 0.03
k_2	-0.206 ± 0.007
$k_{\Phi 1}$	0.430 ± 0.034
$k_{\Phi 2}$	1.139 ± 0.034
$\log(\Phi_0^*)$	-5.79 ± 0.07
χ^2	121.0
ν	77
P_{χ^2}	1.0e–3
$D_{\rm KS}$	0.0096
$P_{\rm KS}$	0.30

extrapolating such empirically derived functional forms outside of the redshift and luminosity ranges over which they are fitted. In particular, it is well known that at $z > 3$ the bright end of the QSO LF flattens again, which is not accounted for in our model.

7 DISCUSSION

7.1 Comparison of number counts to 2QZ

The number counts and LF from 2SLAQ broadly agree with other works, but provide a significant advance in the precision available to constrain the faint end of the QSO LF at $z < 2.6$. We confirm that the 2SLAQ survey sees an excess in counts over the 2QZ fainter than $g \simeq 20.0$. To further examine this, we recalculate the 2SLAQ number counts in identical bins to 2QZ (correcting the difference in passbands using $g - b_J = -0.045$). Brighter than $g \simeq 20.0$ the 2QZ and 2SLAQ QSO number counts agree well. However, we find that the ratios of the differential counts are $N_{\rm 2QZ}(g)/N_{\rm 2SLAQ}(g) = 0.85 \pm 0.03$ and 0.75 ± 0.02 for 0.25 mag bins centred on $g = 20.38$ and 20.63, respectively. The slope of the integrated 2SLAQ number counts at this magnitude is $\simeq$0.36. Thus, a systematic offset in magnitude of $\Delta g \simeq 0.35$ would be sufficient to cause this difference. Such an error must be magnitude-dependent, as there is no visible offset between 2QZ and 2SLAQ brighter than $g \simeq 20$.

There are several possible causes for the observed deficit of faint 2QZ QSOs. First, we check for scale errors in the calibrated photographic photometry, by cross matching the 2QZ input catalogue of stellar objects (Smith et al. 2005) with SDSS imaging data, finding $\sim$600 000 matches to $b_J \simeq 22$. This is only possible in the NGP region of the 2QZ (which also overlaps with 2SLAQ). The SDSS magnitudes are converted to an effective SDSS b_J magnitude by combining the relation $b_J = B - 0.28(B - V)$ (Blair & Gilmore 1982) with the SDSS colour transformations given by Jester et al. (2005) to give

$$b_J = g + 0.116(g - r) + 0.148. \quad (23)$$

This transformation is appropriate for stars, as we are comparing the photometry from the full stellar 2QZ catalogue, not just the objects selected as QSO candidates. A slightly different transformation is appropriate for QSOs (see Jester et al. 2005). We calculate the median magnitude difference $[b_J(\rm SDSS) - b_J(2QZ)]$ in 0.1 mag intervals, as is shown in Fig. 17. This difference between the 2QZ and SDSS magnitudes is almost constant from $b_J = 16$ to 20.85 and is well described by an eighth-order polynomial (solid red line) over this range. At $b_J = 18$–20, $b_J(\rm SDSS) - b_J(2QZ)$ is roughly constant, $\simeq$0.04 mag, and declines to $\simeq$0.01 mag at $b_J = 20.85$. This $\simeq$0.03 scale error between $b_J = 20$ and 20.85 is in the right sense to explain the number count discrepancy, but is an order of magnitude too small.

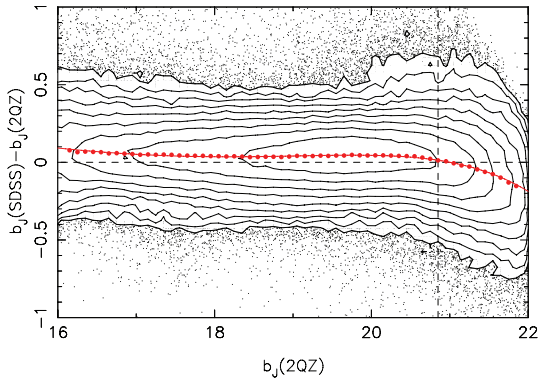

Figure 17. The difference in stellar magnitudes between SDSS and 2QZ in the b_J band, as a function of b_J. The small points and contours show the distribution of $\simeq$600 000 stars in the 2QZ NGP region which also have the SDSS photometry. The contours are spaced logarithmically by 0.25 dex. The vertical dashed line marks the faint limit of the 2QZ survey at $b_J = 20.85$. The large red points show the median $b_J(\rm SDSS) - b_J(2QZ)$ at 0.1 mag intervals. The solid red line shows the best-fitting polynomial to these points.

A second possible cause of the number count difference is that the colour selection of the 2QZ is less complete than was estimated by C04. We match the 2SLAQ QSOs to the 2QZ photometry and find that 95 per cent of 2SLAQ QSOs (at $0.4 < z < 2.1$) would have been selected by 2QZ, independent of b_J. This rules out colour selection as the cause of the number count discrepancy. It could also be the case that as we approach the plate limit, sources are not being detected on the United Kingdom Schmidt Telescope (UKST) plates. When matching 2SLAQ QSOs to the 2QZ photometry, we find that brighter than $g = 20$, 93 ± 3 per cent of 2SLAQ sources can be matched to the 2QZ stellar photometry (those missing are in large part due to holes around bright stars in the 2QZ catalogue). At $g = 20.4$ to 20.8, only 88 ± 3 per cent are matched to 2QZ, indicating that an increasing fraction of sources are missing from the 2QZ catalogue at fainter fluxes, although again, the effect seen is not sufficient to explain the observed discrepancy in the number counts. We suspect that a combination of small photometric calibration errors, missing objects at fainter fluxes and other currently unknown errors together contribute to the discrepancy seen between the 2SLAQ and 2QZ number counts.

7.2 LF models, evolution and downsizing

The break in the QSO LF we have measured in this paper is a gradual flattening which takes place over several magnitudes. Most of this flattening occurs just faintwards of the SDSS QSO LF, but in the region of overlap the SDSS and 2SLAQ LFs are in excellent agreement. The combination of SDSS and 2SLAQ allows us to simultaneously place accurate constraints on both the bright and faint ends of the QSO LF, with errors in the binned LF typically $<$0.1 dex (and often $\simeq$0.02–0.03 dex) over a range of 5–6 mag (i.e.

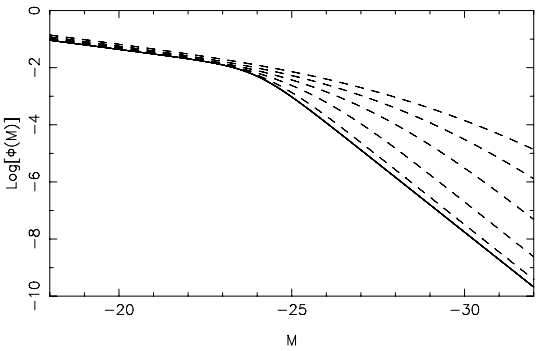

Figure 18. The effect of convolving a double power-law LF with a Gaussian distribution in magnitude. The original double power law (solid line) is convolved with Gaussians of five different widths, $\sigma = 0.5$, 1.0, 1.5, 2.0 and 2.5 mag (dashed lines, bottom to top).

over a factor of 100 in luminosity). With errors of this size, much greater care needs to be taken over systematic errors, as these may dominate over the statistical errors. We find that previous smaller surveys generally agree with the higher precision 2SLAQ+SDSS LF measurements.

When comparing our combined QSO LF to the soft X-ray LF of type 1 AGN measured by Hasinger et al. (2005), we find good agreement near M^*. However, the measured bright-end slope is significantly steeper in the 2SLAQ+SDSS data set than the X-ray data. We find that an α_{ox} which has a much weaker dependence on luminosity than previously measured (e.g. Steffen et al. 2006) provides an improved match between the LFs. Green et al. (2009) find a weaker luminosity dependence for α_{ox}, but this is largely limited to fainter luminosities ($M_B > -23$), and they find a result similar to Steffen et al. at brighter magnitudes. The measured rms scatter in α_{ox} could potentially alter the shape of the LF. In Fig. 18, we plot a fiducial double power-law LF (solid line) and the convolution of this with a Gaussian distribution (dashed lines). The LF retains its shape well away from the break, but the bright-end slope is flattened near the break. The scatter in log (L_X) found by Steffen et al. (2006) is ∼0.3–0.4 dex, corresponding to ∼0.75–1.0 mag. Such a scatter qualitatively provides the correct flattening of the bright end of the QSO LF, although only locally, within ∼2–3 mag of M^*. Of course, the probability distribution function for such a scatter may not be Gaussian, and may also depend on luminosity. Detailed consideration of this is outside the scope of this paper, and would ideally require the measurement of the bivariate X-ray/optical LF for a sample that was largely complete at both wavelengths. However, we do note that if scatter in α_{ox} is the cause of the LF difference, this infers that optical/UV luminosity is the independent variable, and X-ray luminosity is the dependent variable. That is, we need to take the optical LF and convolve it with a Gaussian to match the two, rather than take the X-ray LF and convolve this with a Gaussian. This is as one might expect, given that the optical/UV light originates from the accretion disc, while the X-ray originates from a hot corona above the disc. In fact, it could be argued that both the optical/UV and X-ray luminosities are dependent on the bolometric luminosity, which should directly correlate to the accretion rate. In this case, the dispersion in the bolometric correction to the X-ray must be larger than the dispersion in the bolometric correction to the UV/optical.

The results of Mahony et al. (2009) suggest a second possible explanation of the flatter bright-end slope of the X-ray LF. They find that the fraction of AGN in the *ROSAT* All Sky Survey Bright Source Catalogue (BSC) which is detected at radio wavelengths by the National Radio Astronomy Observatory VLA Sky Survey (Condon et al. 1998) and the Sydney University Molonglo Sky Survey (Mauch et al. 2003) increases with increasing redshift. At $z > 1$, almost all QSOs in the BSC are detected in these radio surveys. The natural explanation of this is that the very luminous high-redshift QSOs in the sample are having their X-ray flux boosted by a jet component, which may also be Doppler boosted by beaming. In contrast, the radio-detected fraction (to the same radio flux limit) of optically bright QSOs is no more that 25 per cent (Jiang et al. 2007). Therefore, the number of QSOs at the bright end of the X-ray LF will be boosted relative to the number in the optical.

The qualitative impression of the LF evolution (seen in Figs 7 and 9) is of a consistent shape where the characteristic luminosity shifts with redshift. This is the classical PLE seen in previous optical samples. A very different impression is obtained from Fig. 10. Here we see that the space density of fainter QSOs peaks at lower redshift than that of high-luminosity QSOs. This is equivalent to the AGN downsizing seen in X-ray samples (e.g. Barger et al. 2005), although it has not been convincingly seen in optical samples until now. Bongiorno et al. (2007) find that their optical LF is better fit by an LDDE model than PLE, but do not provide any errors on their model fits to directly assess the significance of downsizing.

Such downsizing immediately rules out PLE, which due to its functional form peaks in space density at the same redshift for every luminosity. Direct fitting of models to the unbinned QSO LF confirms the disagreement with PLE, although we note that the best-fitting PLE model plotted in Fig. 9 is relatively close to the data in all but the highest redshift interval. The disagreement with PLE is much clearer in Fig. 10. The discord between PLE and the 2SLAQ LF is most prominent at low luminosities and high redshifts. This is exactly the point at which the downsizing is most notable in the binned LF. There is also some disagreement at $z \sim 1.5$ and $M_g \sim -24$, where the errors on the LF are particularly small given the large numbers of QSOs per bin.

A much improved fit is obtained if we use an LDDE model. While the functional form of Hasinger et al. (2005) does not provide a reduction in χ^2, if we modify this to use a smooth functional form (equations 17 and 18) a much better fit is obtained. However, this is still a relatively poor fit ($\chi^2/\nu = 146.8/77$) and also behaves badly outside of the fitted range of the data. A model which combines luminosity evolution and simple density evolution (our LEDE model) provides a further improvement to the fit with $\chi^2/\nu = 121.0/77 (P_{\chi^2} = 0.001)$ and a KS test which is formally consistent at the 1σ level ($P_{KS} = 0.30$). The LEDE model is the best match to our combined 2SLAQ+SDSS data set for both the χ^2 and KS tests. Even in this case the χ^2 is still formally a poor fit, it is worth considering whether this is due to residual systematic errors. To do this, we carry out the binned χ^2-test on the best-fitting models, adding a fixed fractional error in quadrature to the statistical error on Φ in each bin. We then determine the systematic error required to make the models acceptable at the 5 per cent level (i.e. $P_{\chi^2} = 0.05$). For the PLE model, a global 12 per cent systematic error is required to achieve an acceptable match, while for the LDDE and LEDE models this is only 6 and 4 per cent, respectively.

If we fit the LF in narrow magnitude intervals, we find further evidence for downsizing (e.g. Fig. 15). Even at relatively bright magnitudes ($M_g > -24$), the redshift at which the space density of QSOs peaks increases with luminosity, and the peak is well below the maximum redshift of our sample, where completeness starts to decline. We find that this trend is similar to that found by the fit of the LDDE model to the full sample (dashed black line in Fig. 15). In comparison, the trends found by Bongiorno et al. (2007; Fig. 15,

green dot–dashed line) and Hasinger et al. (2005; Fig. 15, red dot–dashed line), fitting a similar LDDE model to VVDS and X-ray data, respectively, were somewhat flatter, although it is not clear whether this difference is significant. The maximum z_c in the best-fitting model of Hasinger et al. (2005) is only $z = 1.42 \pm 0.11$ which disagrees with the peak in the space density of high-luminosity optical QSOs (e.g. R06 and this work). Such a disagreement is likely to be due to the relatively low number of X-ray objects at the brightest luminosities. At the lowest luminosities, there is good agreement between our estimated z_p and those estimated from the other works. There are various other evolutionary trends which are inconsistent with the simple PLE model; these include evolution in the bright-end slope α and evolution in Φ^* (see Fig. 16).

Recent simulations (e.g. Hopkins et al. 2006) suggest that the faint-end slope of the QSO LF is set by the light curves of QSOs fainter than their peak luminosity. These hydrodynamical simulations find that the faint-end slope is a function of peak luminosity and, indirectly, a function of redshift, as the distribution of peak luminosities shifts towards higher luminosity at higher redshift (at least up to $z \simeq 2.5$). Our best-fitting models show no evidence of faint-end slope evolution (e.g. Fig. 16) and find a slope of $\beta = -1.38 \pm 0.03$. However, this is consistent with the model faint-end slopes of Hopkins et al. at redshift $\gtrsim$0.5, as it is only at the lowest redshifts that the faint-end slope is predicted to evolve appreciably. In fact, the lowest redshift bins in Fig. 16(b) do show a steeper slope, more consistent with the predicted turnup (see fig. 3 of Hopkins et al. 2006).

Further developments by Hopkins et al. (2008) placed the above light curves into a cosmological context, combining evolving dark matter halo mass functions, halo occupation distributions and merger rates to predict the evolution of the QSO population. This model gives reasonably good agreement with a combination of recent LF measurements, improving on earlier models (e.g. Wyithe & Loeb 2002). The LF presented here has the best combination of dynamic range and precision of any yet measured. As such, it will provide further constraints on QSO formation models.

We find highly significant (99.9 per cent) evolution of the bright-end slope of the LF, which steepens from $\alpha \simeq -3.0$ at $z \sim 0$ to $\alpha \simeq -3.5$ at $z \sim 2.5$. This strengthens the previous evidence for such a trend (e.g. Goldschmidt & Miller 1998), and is in general agreement with the evolution seen by Hopkins et al. (2007), although in detail the form of the evolution is somewhat different (see Fig. 16a). A naive direct mapping from the evolving dark matter halo mass function would also produce such an evolution in the bright-end slope. QSOs typically populate similar mass dark matter haloes at all redshifts $z < 2.5$ (e.g. Croom et al. 2005). Therefore, as the mass function becomes steeper at higher mass (relative to the break in the mass function) and the break in the mass function moves to lower mass at higher redshift, the typical QSO host mass moves to a steeper part of the mass function with increasing redshift. However, at $z > 2.5$ the bright end of the LF is seen to flatten again (R06), in disagreement with a naive mapping from the halo mass function. The more complex models of Hopkins et al. (2008) appear to reproduce such trends.

8 SUMMARY

In this paper, we present the optical QSO LF with unprecedented precision and dynamic range. We do this by combining the 2SLAQ and SDSS data sets to probe both the faint and bright ends of the LF at $z < 2.6$. Although the evolution of QSO LF appears very similar to PLE, we find significant departures from this form of evolution. A form of LDDE provides a better fit to the LF, but we find that this can still be improved upon. We find that the bright-end slope and Φ^* both show significant evolution, so use a modified PLE model with added density evolution which we call LEDE. The LEDE model produces the best fit of all models investigated, although a systematic error of 4 per cent is required to make the data formally consistent (at the 2σ level) with the model in our χ^2-test. To make further progress in our understanding of the QSO LF, new measurements at faint magnitudes and high redshift ($z > 3$) need to be made, making an accurate measurement of the faint-end slope and better constraining the bright-end slope. The AUS survey (Croom et al., in preparation), currently underway on the Anglo-Australian Telescope, aims to do this, reaching an equivalent magnitude limit to 2SLAQ, but up to $z \sim 5.5$. As improvements are made to photometric QSO samples, they will also provide the opportunity to investigate the faint end of the QSO LF (e.g. Richards et al. 2009). Further progress in the optical is also dependent on our ability to account for the contamination in optical samples, particularly at redder wavelengths. If we can do this, then new larger area optical imaging surveys [e.g. Large Synoptic Survey Telescope (LSST); Ivezić et al. 2008] will allow substantial improvements in our characterizing of the evolution of AGN.

ACKNOWLEDGMENTS

The 2SLAQ survey is based on observations made with the Anglo-Australian Telescope and the SDSS. We warmly thank all the present and former staff of the Anglo-Australian Observatory for their work in building and operating the 2dF facility. The 2QZ is based on observations made with the Anglo-Australian Telescope and the UKST.

Funding for the SDSS and SDSS-II has been provided by the Alfred P. Sloan Foundation, the participating institutions, the National Science Foundation, the US Department of Energy, the National Aeronautics and Space Administration, the Japanese Monbukagakusho, the Max Planck Society and the Higher Education Funding Council for England. The SDSS web site is http://www.sdss.org/.

The SDSS is managed by the Astrophysical Research Consortium for the participating institutions. The participating institutions are the American Museum of Natural History, Astrophysical Institute Potsdam, University of Basel, University of Cambridge, Case Western Reserve University, University of Chicago, Drexel University, Fermilab, the Institute for Advanced Study, the Japan Participation Group, Johns Hopkins University, the Joint Institute for Nuclear Astrophysics, the Kavli Institute for Particle Astrophysics and Cosmology, the Korean Scientist Group, the Chinese Academy of Sciences (LAMOST), Los Alamos National Laboratory, the Max Planck Institute for Astronomy (MPIA), the Max Planck Institute for Astrophysics (MPA), New Mexico State University, Ohio State University, University of Pittsburgh, University of Portsmouth, Princeton University, the United States Naval Observatory and the University of Washington.

SMC acknowledges the support of an Australian Research Council QEII Fellowship and a J G Russell Award from the Australian Academy of Science. GTR acknowledges support from an Alfred P. Sloan Research Fellowship. NPR and DPS acknowledge the support of National Science Foundation grant AST06-07634. MAS acknowledges the support of National Science Foundation grant AST-0707266.

REFERENCES

Abazajian K. et al., 2003, AJ, 126, 2081
Alexander D. M. et al., 2003, AJ, 126, 539
Barger A. J. et al., 2005, AJ, 129, 578
Blair M., Gilmore G., 1982, PASP, 94, 742
Blanton M. R. et al., 2003, AJ, 125, 2348
Bongiorno A. et al., 2007, A&A, 472, 443
Boyle B. J., Shanks T., Peterson B. A., 1988, MNRAS, 235, 935 (BSP88)
Boyle B. J., Fong R., Shanks T., Peterson B. A., 1990, MNRAS, 243, 1 (BFSP90)
Boyle B. J., Jones L. R., Shanks T., 1991, MNRAS, 251, 482 (BJS91)
Boyle B. J., Griffiths R. E., Shanks T., Stewart G. C., Georgantopoulos I., 1993, MNRAS, 260, 49
Boyle B. J., Shanks T., Croom S. M., Smith R. J., Miller L., Loaring N., Heymans C., 2000, MNRAS, 317, 1014
Braccesi A., Zitelli V., Bonoli F., Formiggini L., 1980, A&A, 85, 80
Condon J. J., Cotton W. D., Greisen E. W., Yin Q. F., Perley R. A., Taylor G. B., Broderick J. J., 1998, AJ, 115, 1693
Cowie L. L., Songaila A., Hu E. M., Cohen J. G., 1996, AJ, 112, 839
Cristiani S., Vio R., 1990, A&A, 227, 385
Croom S. M., Smith R. J., Boyle B. J., Shanks T., Loaring N. S., Miller L., Lewis I. J., 2001, MNRAS, 322, L29
Croom S. M., Smith R. J., Boyle B. J., Shanks T., Miller L., Outram P. J., Loaring N. S., 2004, MNRAS, 349, 1397 (C04)
Croom S. M. et al., 2005, MNRAS, 356, 415
Croom S. M. et al., 2009, MNRAS, 392, 19 (C09)
Di Matteo T., Springel V., Hernquist L., 2005, Nat, 433, 604
Elvis M. et al., 1994, ApJS, 95, 1
Fan X. et al., 2001, AJ, 121, 54
Fukugita M., Ichikawa T., Gunn J. E., Doi M., Shimasaku K., Schneider D. P., 1996, AJ, 111, 1748
Gavignaud I. et al., 2006, A&A, 457, 79
Giacconi R. et al., 2002, ApJS, 139, 369
Goldschmidt P., Miller L., 1998, MNRAS, 293, 107
Green P. J. et al., 2009, ApJ, 690, 644
Gunn J. E. et al., 1998, AJ, 116, 3040
Gunn J. E. et al., 2006, AJ, 131, 2332
Hasinger G. et al., 2001, A&A, 365, L45
Hasinger G., Miyaji T., Schmidt M., 2005, A&A, 441, 417
Hewett P. C., Foltz C. B., Chaffee F. H., 1993, ApJ, 406, L43
Hopkins P. F., Hernquist L., Cox T. J., Di Matteo T., Martini P., Robertson B., Springel V., 2005a, ApJ, 630, 705
Hopkins P. F., Hernquist L., Cox T. J., Di Matteo T., Robertson B., Springel V., 2005b, ApJ, 630, 716
Hopkins P. F., Hernquist L., Cox T. J., Robertson B., Di Matteo T., Springel V., 2006, ApJ, 639, 700
Hopkins P. F., Richards G. T., Hernquist L., 2007, ApJ, 654, 731
Hopkins P. F., Hernquist L., Cos T. J., Keres D., 2008, ApJS, 175, 356
Ivezić Ž. et al., 2008, preprint (arXiv:0805.2366)
Jester S. et al., 2005, AJ, 130, 873
Jiang L. et al., 2006, AJ, 131, 2788
Jiang L., Fan X., Ivezić Ž., Richards G. T., Schneider D. P., Strauss M. A., Kelly B. C., 2007, ApJ, 656, 680
Juneau S. et al., 2005, ApJ, 619, 135
Koo D. C., Kron R. G., 1988, ApJ, 325, 92 (KK88)
Kormendy J., Richstone D., 1995, ARA&A, 33, 581
Lewis I. J. et al., 2002, MNRAS, 333, 279
Mahony E. K., Croom S. M., Boyle B. J., Edge A. C., Mauch T., Sadler E. M., 2009, MNRAS, submitted
Marshall H. L., Tananbaum H., Avni Y., Zamorani G., 1983, ApJ, 269, 35
Mauch T., Murphy T., Buttery H. J., Curran J., Hunstead R. W., Piestrzynski B., Robertson J. G., Sadler E. M., 2003, MNRAS, 342, 1117
Miyaji T., Hasinger G., Schmidt M., 2001, A&A, 369, 49
Noeske K. G. et al., 2007, ApJ, 660, L47
Oke J. B., Gunn J. E., 1983, ApJ, 266, 713
Osmer P., 1982, ApJ, 253, 28
Page M. J., Carrera F. J., 2000, MNRAS, 311, 433
Peacock J. A., 1983, MNRAS, 202, 615
Richards G. T. et al., 2005, MNRAS, 360, 839 (R05)
Richards G. T. et al., 2006, AJ, 131, 2766 (R06)
Richards G. T. et al., 2009, ApJS, 180, 67
Sanders D. B., Soifer B. T., Elias J. H., Neugebauer G., Matthews K., 1988, ApJ, 328, L35
Schlegel D. J., Finkbeiner D. P., Davis M., 1998, ApJ, 500, 525
Schmidt M., 1972, ApJ, 176, 273
Schmidt M., Green R. F., 1983, ApJ, 269, 352
Schmidt M., Schneider D. P., Gunn J. E., 1995, AJ, 110, 68
Schneider D. P. et al., 2003, AJ, 126, 2579
Schneider D. P. et al., 2007, AJ, 134, 102
Smith J. R., Croom S. M., Boyle B. J., Shanks T., Miller L., Loaring N. S., 2005, MNRAS, 359, 57
Steffen A. T., Strateva I., Brandt W. N., Alexander D. M., Koekemoer A. M., Lehmer B. D., Schneider D. P., Vignali C., 2006, AJ, 131, 2826
Stoughton C. et al., 2002, AJ, 123, 485
Tremaine S. et al., 2002, ApJ, 574, 740
Ueda Y., Akiyama M., Ohta K., Miyaji T., 2003, ApJ, 598, 886
Warren S. J., Hewett P. C., Osmer P. S., 1994, ApJ, 421, 412
Wisotzki L., 2000, A&A, 353, 861
Wolf C., Wisotzki L., Borch A., Dye S., Kleinheinrich M., Meisenheimer K., 2003, A&A, 408, 499
Worsley M. A., Fabian A. C., Barcons X., Mateos S., Hasinger G., Brunner H., 2004, MNRAS, 352, L28
Wyithe J. S. B., Loeb A., 2002, ApJ, 581, 886
York D. G. et al., 2000, AJ, 120, 1579
Zheng X. Z., Bell E. F., Papovich C., Wolf C., Meisenheimer K., Rix H-W., Rieke G. H., Somerville R., 2007, ApJ, 661, L41

This paper has been typeset from a TEX/LATEX file prepared by the author.